

Insights into topaz rhyolite magma evolution from mafic enclaves and
melt inclusion volatile SIMS analyses, China Hat, SE Idaho

by
Ryan Goldsby

A thesis
submitted in partial fulfillment
of the requirements for the degree of
Master of Science in the Department of Geosciences
Idaho State University
Spring 2017

In presenting this thesis in partial fulfillment of the requirements for an advanced degree at Idaho State University, I agree that the Library shall make it freely available for inspection. I further state that permission to download and/or print my thesis for scholarly purposes may be granted by the Dean of the Graduate School, Dean of my academic division, or by the University Librarian. It is understood that any copying or publication of this thesis for financial gain shall not be allowed without my written permission.

Signature _____

Date _____

Committee Approval

To the Graduate Faculty:

The members of the committee appointed to examine the thesis of RYAN GOLDSBY find it satisfactory and recommend that it be accepted.

Michael McCurry,

Major Advisor

David Pearson,

Committee Member

Rene Rodriguez,

Graduate Faculty Representative

Acknowledgements

I would like to first thank my committee, Drs. Mike McCurry, Dave Pearson, and Rene Rodriguez. Without their insight and help throughout the years, this thesis would never have come together in any intelligible fashion.

Many people were of huge assistance in completing my research, and I hope I am not leaving anyone out here:

Dr. Eric Christiansen, BYU, obtained the XrF data for me, and had insightful ideas about the data.

Dr. Jacob Lowenstern, USGS, helped with getting the ball rolling on my melt inclusion work, and graciously let us use his lab in the early stages of research.

Dr. Kurt Roggensack, ASU, aided immensely with homogenization of melt inclusions, and provided valuable insight regarding preparation of the melt inclusions.

Dr. Axel Schmitt, Heidelberg University, Germany, helped in assistance and preparation of melt inclusions, taught me much about melt inclusions, SIMS, and Germany. He aided in the use of the ion microprobe, and showed me around much of the Heidelberg area. He also graciously gave me a place to stay in Germany for several days while I was figuring out the hostel situation.

The people of Pocatello and Idaho State University have always helped immensely both in and out of school, and are far too numerous to name individually. A few that need mentioned are:

Kate and Mel in the office. Without them I would not have gotten paid, gotten travel figured out, nor figured out how to use grant money.

Dr. Paul Link helped inspire my interest for geology and science in general and field camp are some of my favorite geology memories.

Fellow ISU students have made my time here at ISU memorable, and have inspired insightful discussion, both geologic and other, often over a beer (or three).

Finally, my parents have been continually supportive, regardless of how many weeks go by without them hearing a word from me.

This research was supported by an ISU COSE grant and the ISU Geosciences Geslin Fund.

Table of Contents

List of Figures	vii
List of Tables	viii
ABSTRACT	ix
Chapter 1: INTRODUCTION	1
Problem Statement	1
Geologic setting	4
The Blackfoot Volcanic Field	9
Preexisting model for the BVF	14
Chapter 2: METHODS	16
Field methods	16
Sample Preparation Methods	17
Thin Sections	17
XrF methods	19
Melt inclusion preparation methods	19
Microanalysis (EMP and SIMS) methods	21
Chapter 3: RESULTS	24
Enclaves	24
Distribution and morphology	24
Petrographic features	27
Bulk geochemistry	29
Melt inclusions	31
Morphology	31
EMP results	32
SIMS results	39
Chapter 4: DISCUSSION/INTERPRETATIONS	44
Preferred cross section model	44
Enclave source	45
Melt inclusion interpretations	48
MI normative mineral interpretations	50
Vapor Saturation	53
Amphibole barometers	55

Model for the BVF	57
Significance for geothermal potential	60
Chapter 5: CONCLUSIONS	62
Future work.....	63
Lithium source.....	63
North Dome Field	64
REFERENCES	66
APPENDIX	76

List of Figures

Figure 1- DEM hillshade of BVF.....	3
Figure 2- Basement map of region	5
Figure 3- Thrust fault relations in region	8
Figure 4- Google Earth image of SDF	10
Figure 5- Picture of tephra deposit underlying China Hat.....	11
Figure 6- Paragenetic interpretation diagram	12
Figure 7- Nd, Sr isotopic diagram.....	14
Figure 8- Previous conceptual model	15
Figure 9- Sample locations.....	18
Figure 10- Quartz crystals in epoxy disk	23
Figure 11- Samples of enclave textures.....	26
Figure 12- Zoned plagioclase in enclave	28
Figure 13- Clinopyroxene phenocryst in enclave.....	28
Figure 14- Ocellar quartz in mixing zone	28
Figure 15- Mixing zone between enclave and rhyolite.....	28
Figure 16- TAS diagram with enclave and BVF data	29
Figure 17- Homogenized melt inclusion	31
Figure 18- Melt inclusions with small capillaries	32
Figure 19- Effect of silica adjustment on melt inclusions.....	34
Figure 20- Silica adjusted EMP results	37
Figure 21- SIMS volatile analysis results.....	39
Figure 22- SIMS volatile analysis results.....	43
Figure 23- TAS diagram with enclave results.....	47
Figure 24- Q-An-Or ternary diagram showing the effects of H ₂ O and pressure	50
Figure 25- Melt inclusion group elemental covariation diagram	52
Figure 26- Pressure vs. CO ₂ solubility plot	55
Figure 27- Model of BVF	59

List of Tables

Table 1- Sample Locations	19
Table 2- Enclave texture descriptions.....	25
Table 3- Enclave major and trace element analyses	30
Table 4-Normalized EMP major element data	35
Table 5-SiO ₂ adjusted major element data	36
Table 6- SIMS volatile analyses	40
Table 7-CIPW norm calculations of melt inclusion populations.....	51
Table 8- Application of amphibole barometers.....	57

ABSTRACT

To better constrain topaz rhyolite petrogenesis and to further evaluate the Blackfoot Volcanic Field (BVF) of SE Idaho for geothermal potential, mafic magmatic enclaves and quartz phenocrysts were collected from the rhyolite following thorough field examination. Thin sections were obtained from the enclaves and bulk geochemical analyses were performed. Quartz-hosted melt inclusions were studied and prepared for EMP and SIMS analyses.

Mafic enclaves occur much more abundantly in the China Cap lava dome compared to the China Hat dome. Hand sample and petrographic analyses show textures indicative of magma mixing. Geochemical trends are highly linear and indicate end-member mixing between topaz rhyolite and primitive, mantle-derived basalt. Melt inclusions are <100 μm , are generally ellipsoidal in geometry, and either appear homogeneous or contain vapor bubbles. Melt inclusion SIMS volatile analyses indicate three different populations of melt, designated by groupings of water content. The lowest water content group is interpreted to be leaked and therefore not represent pre-eruptive conditions. The two other groups of water contents, at 2.7 weight % H_2O , and at 4.5 weight % H_2O indicate distinct regions of rhyolitic melt. Normative mineral assemblages of the two groups may indicate volatile undersaturation of magma during time of melt inclusion capture. A new amphibole barometer is applied to amphibole analyses from an earlier study, indicating amphibole equilibration at 12.18 ± 1.96 km.

These results are used to build upon a model for the BVF, where a dynamic magmatic system is evolving at depth, periodically mixing discrete regions of magma

prior to eruption. Inputs from deeper sources bring primitive mantle-derived magma which contribute heat and mass into the system, driving mixing of high-melt regions. The enrichment of the topaz rhyolite is driven by extreme fractional crystallization, enhanced by partial melting of the solidifying rhyolite. Fluids from the degassing magma system may contribute to areas of high heat flow near the BVF.

Chapter 1: INTRODUCTION

Problem Statement

The goal of this thesis is to better constrain the dynamic evolution of the topaz rhyolites of the bimodal Blackfoot Volcanic Field (BVF) (Figure 1) of SE Idaho, in an attempt to better understand the generation of highly evolved rhyolites. To understand the dynamic evolution of the BVF magmatic system, this study focuses on two aspects of rhyolite genesis: (1) the roles that mafic magma recharge and mixing played in the evolution of these rhyolites; and (2) volatile incompatible element evolution of the rhyolitic melt. A better understanding of the magma and fluid evolution of this young volcanic system will also help evaluate the BVF as a source of potential geothermal energy in the area. The rhyolites of the southern dome field (SDF) (or China Hat dome field) are the central focus of this thesis, which are classified as topaz-rhyolites due to their enrichment in incompatible trace elements and fluorine (Dayvault et al., 1984; Christiansen et al., 1986)

Mafic enclaves and quartz-hosted melt inclusions within the SDF rhyolite were collected and analyzed to test multiple working hypotheses about the development of this topaz-rhyolite:

- (1) The mafic enclaves within the rhyolite represent primitive olivine tholeiitic basaltic magma that was intruded into the magma chamber prior to the eruption of the rhyolite. These olivine tholeiitic basaltic enclaves would share a source with the surrounding olivine tholeiitic basalts of the Blackfoot Volcanic Field.

- (2) The mafic enclaves represent evolved mafic rocks intruded into the chamber prior to eruption. This evolved mafic source would suggest a distinct evolving mafic magmatic reservoir that is able to interact with the rhyolite reservoir. This has been suggested for Quaternary rhyolites on the Eastern Snake River Plain (e.g. Ganske, 2006; Ganske and McCurry, 2007).
- (3) The mafic enclaves represent xenoliths captured by the rhyolite during the storage/ascent of the magma. The enclaves would in this case not be from magma mixing, but would instead be captured wall-rock material.
- (4) The rhyolites of the BVF are the product of a rapid assembly of multiple magma reservoirs prior to eruption.
- (5) This magma reservoir at depth is the source of hot fluids and lithium identified in areas with high heat flow and high lithium concentration anomalies to the NNE of the BVF, which may play a role in the geothermal potential of the area (Welhan, 2016).

The purpose of testing these aspects of rhyolite petrogenesis is to confront the problem of rhyolite production in continental settings, where many different origins of silicic volcanism have been suggested, including: (1) partial melting of continental crust (e.g. Christiansen et al., 1986); (2) extreme fractional crystallization (McCurry et al., 2008) via melt extraction from evolving crystal-rich, “mushy” magma chambers (Bachmann and Bergantz, 2008); (3) partial melting of associated precursor gabbroic intrusions (Christiansen and McCurry, 2008); (4) recycling and remobilization of intrusive silicic protoliths generated by any of these previous methods (Bindeman and Simakin,

2014). The Blackfoot Volcanic Field (BVF) provides a unique opportunity to study the development of a young, highly evolved, topaz rhyolite.

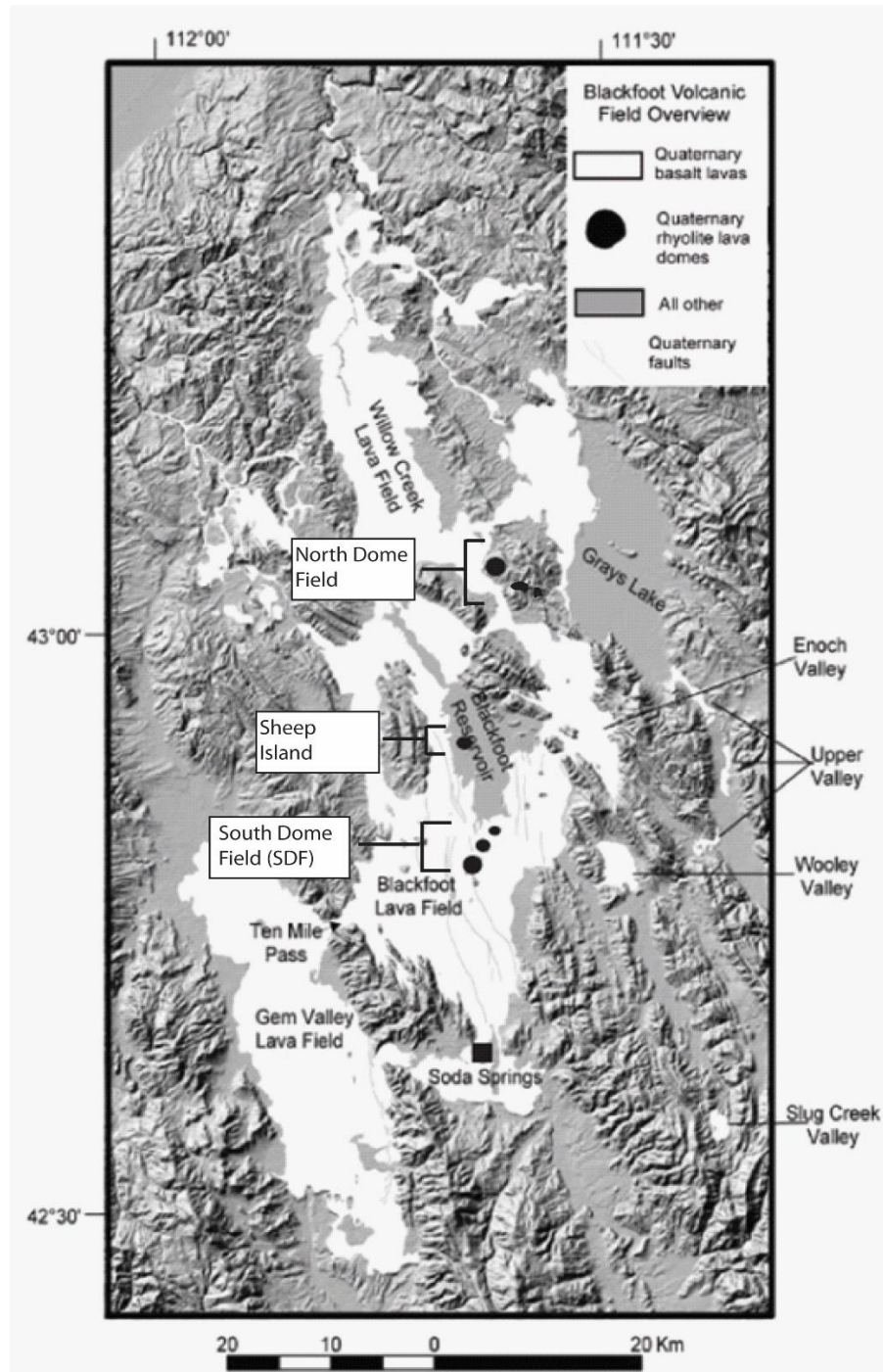


Figure 1- Hillshade map of the Blackfoot Volcanic Field and other interconnected lava fields. Modified from Ford (2005) and Pickett (2004).

Geologic setting

The BVF located in SE Idaho lies near the intersection of multiple basement provinces.

The oldest rocks in SE Idaho are the Archean Wyoming cratonal rocks that constitute a significant portion of western Laurentia (e.g. Foster et al., 2006; Karlstrom et al., 2005). The western boundary of the Wyoming craton is the Farmington Zone, a group of 2.45 Ga rocks metamorphosed at 1.7 Ga (Mueller et al., 2011). The rifting of Rodinia began ~750 Ma and provided space for syn-rift Neoproterozoic to early Paleozoic sediments to accumulate on the western margin of what is now North America (e.g. Yonkee et al., 2014). In SE Idaho, these rocks consist of the Pocatello Formation and the Brigham Group (Link et al., 1993). Post-rift passive margin sedimentation continued until mid-Devonian time.

Following passive margin sedimentation, folding and thrusting associated with the Sevier orogeny was initiated in Early Cretaceous time, and continued in the area until the early Cenozoic. Sevier thrusting juxtaposed Proterozoic and younger rocks many kilometers eastward along a series of thrust sheets, now exposed in SE Idaho. The BVF is located between the Paris and Meade thrusts (Figure 3), which were active during the Early Cretaceous (Crittenden, 1972; Yonkee, 2005). See Yonkee and Weil (2015) for an extensive overview of the Sevier orogeny and deformation.

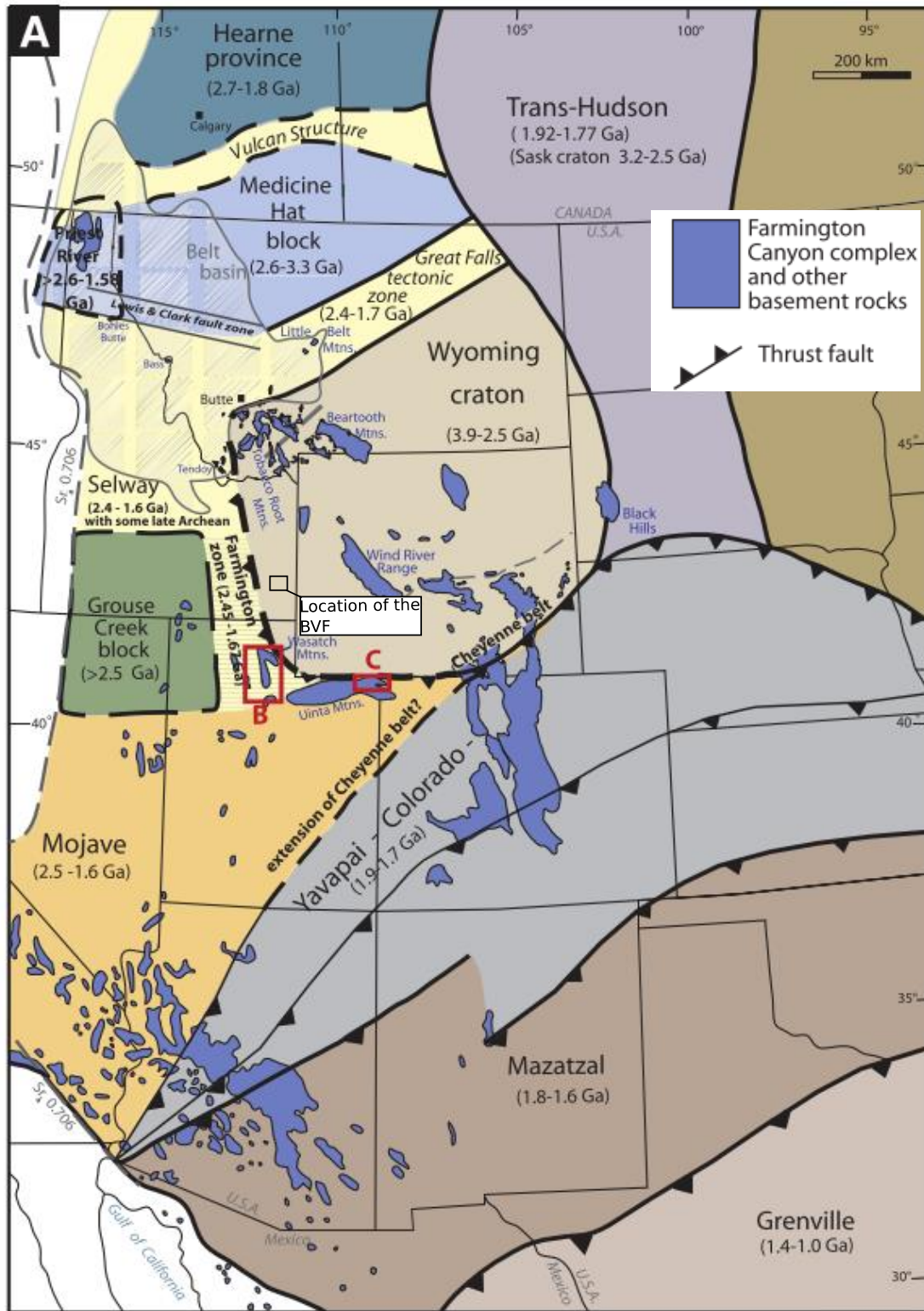


Figure 2- Location of basement provinces and outcrops near the location of the Blackfoot Volcanic Field. This map is modified from Mueller et al. (2011) and shows a Paleoproterozoic “Farmington Zone” separating the Grouse Creek Block from the Wyoming craton.

Extension in SE Idaho began in the mid Miocene (~16 Ma) and accommodated 15-20 percent extension along west-dipping normal faults (Rodgers et al., 2002). The BVF field is in the hanging wall of a west-dipping normal fault, with the Aspen Range to the east of the volcanic field forming the footwall of this fault (Figure 4). Evidence for Quaternary normal faulting within the field is recorded by numerous normal faults that cut the basalt and a small part of the southern-most rhyolite dome (China Hat) (e.g. Dayvault et al., 1984; Polun, 2011).

The BVF lies near a change in extension direction, with dominantly N-S striking normal faults south of the BVF, to NW-SE striking north of the BVF. This change in strike direction follows the change in direction of pre-existing thrusting geometry (i.e. the Wyoming salient), and interestingly a zone of NW-SE striking normal faults and another zone of right stepping N-S striking normal faults intersect at the SDF (McCurry et al., 2015). This intersection of faulting directions may be accommodating sinistral displacement of the non-extending Snake River Plain to the north with the actively extending Basin and Range province to the south, as recorded by GPS data (Payne et al., 2012).

However, normal faults can also form as the result of dike injection into the crust, and the Quaternary normal faults in the BVF have also been suggested to be the result of dike injection. Polun (2011), based on mapping and analytical models, suggested that a mass of dikes 200 – 600 m wide is located at a depth of 1 – 2 km in the crust beneath of BVF. This diking model differs considerably from the tectonic model of McCurry et al. (2015).

Neogene to present volcanism in the region is dominated by the Yellowstone Hotspot track (e.g. Pierce and Morgan, 1992). Yellowstone hotspot volcanism began around 17 Ma with the eruption of the Steens basalt in SE Oregon, followed by a NE trending track of volcanism leading to the current position of Yellowstone National Park in NW Wyoming. This hotspot track is characterized by a bimodal suite of volcanic rocks, beginning with large-volume, caldera-forming rhyolitic eruptions. Post-dating these early rhyolites are primitive olivine tholeiitic basalts which cover the majority of the plain, coeval with high-silica rhyolite domes. The source of the volcanism is most commonly attributed to a deep mantle plume (e.g. (Morgan, 1971; Pierce and Morgan, 2009; Anders et al., 2014), although non-plume models have been suggested as well (e.g. Foulger et al., 2015). The Eastern Snake River Plain is dotted by several Quaternary rhyolites dominantly derived from fractional crystallization processes. (McCurry et al., 2008), and postdate main stage rhyolitic volcanism by several million years.

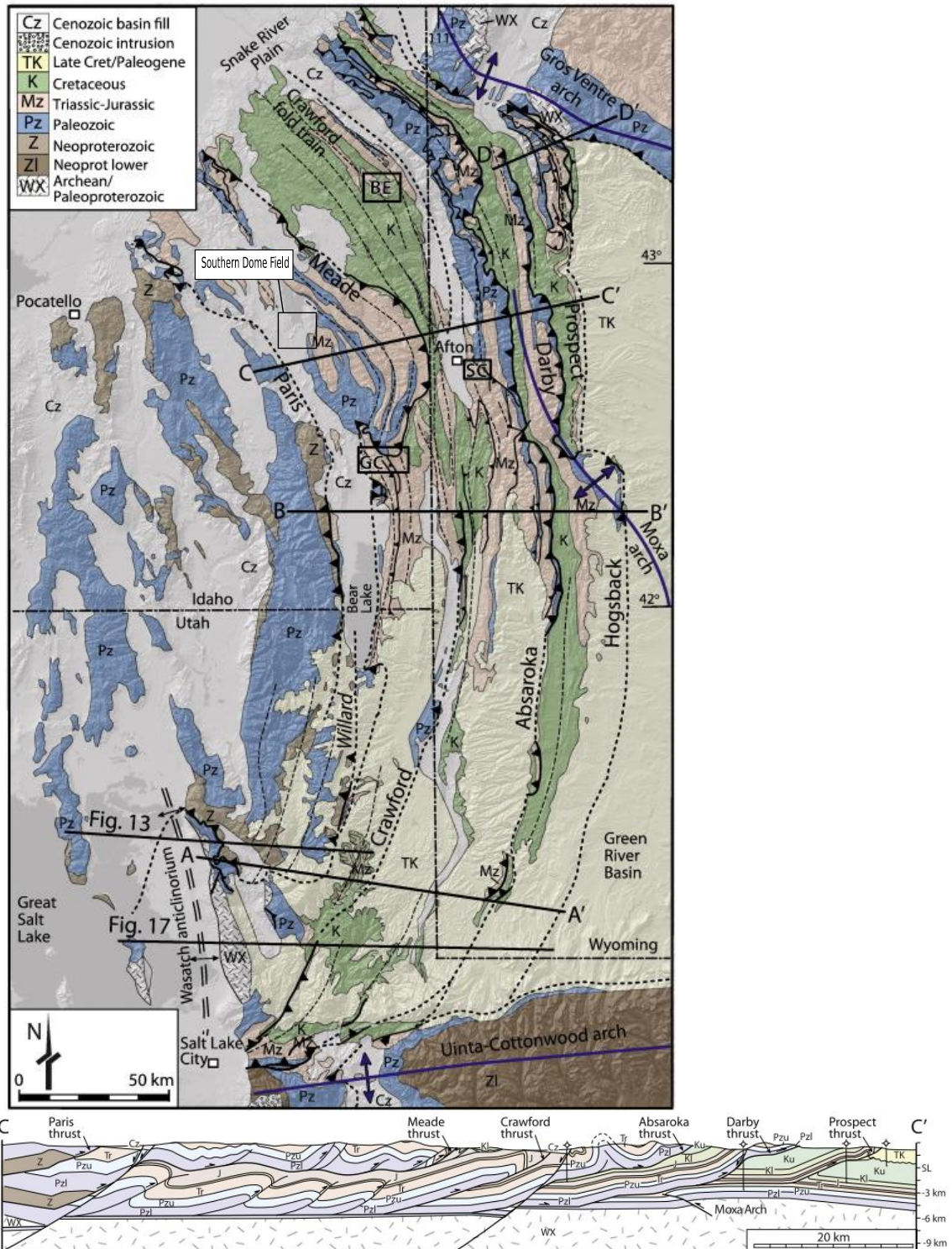


Figure 3- Location of the Southern Dome Field in relation to thrust faults and Paleozoic through Precambrian rocks. The BVF lies in the hanging wall of the Meade Thrust. Cross section C – C' from Yonkee and Weil (2015) is shown. Modified from Yonkee and Weil, 2015.

The Blackfoot Volcanic Field

The BVF of SE Idaho is a bimodal volcanic field consisting of widespread basaltic volcanism and clusters of rhyolite lava domes (Mansfield, 1927; Fiesinger et al., 1982) (Figure 1). The basalts of the field are primitive to moderately evolved olivine tholeiites, similar in composition and mineralogy to basalts of the Eastern Snake River Plain (ESRP) (Fiesinger et al., 1982; Pickett, 2004). However, some unique trachy-andesitic basalts exist in nearby Slug Valley, which Fiesinger et al. (1982) suggest may be evidence for mantle heterogeneity beneath the area. Though similar in composition to ESRP basalts, the rift-dominated style of volcanism in the BVF differs considerably from ESRP basaltic-shield-dominated style volcanism, and is more similar to that of Basin and Range-style volcanism (Pickett, 2004).

Rhyolite lava domes occur in three separate fields: the Northern, Southern (or Sheep Island), and Central Dome Fields, though most studies have been focused on the Southern Dome Field, also called the China Hat Dome Field (CHDF) (Figure 1; Figure 4). The rhyolites of the SDF are highly evolved (Dayvault et al., 1984; Heumann, 1999), and classified as topaz rhyolites based on their characteristic enrichment in incompatible trace elements and fluorine (Christiansen et al., 1986; Ford, 2005).

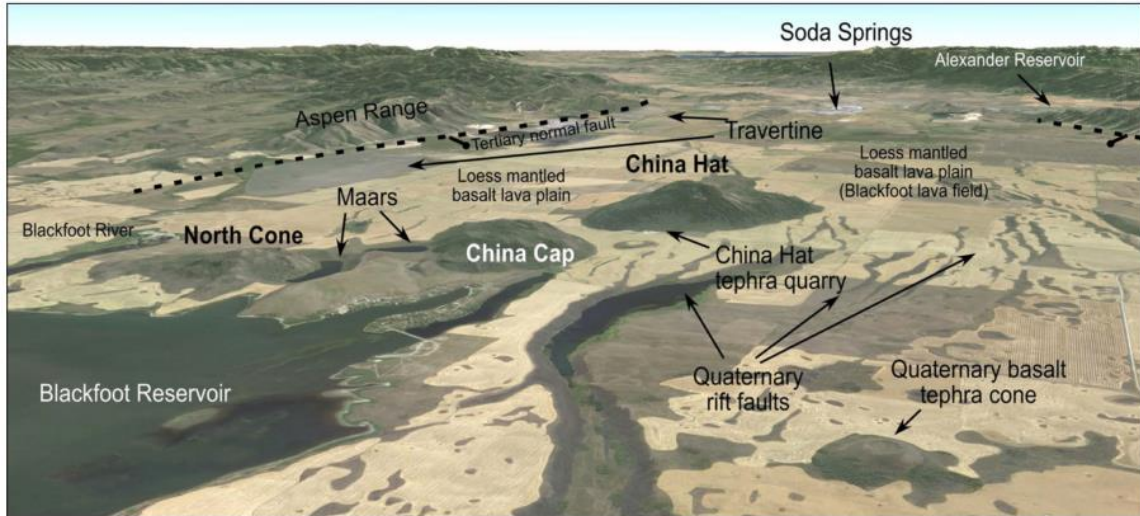


Figure 4- Google Earth image of the Southern Dome Field looking SE. Note the Aspen Range to the east and the numerous quaternary faults in offsetting basalt in the valley. From McCurry et al., 2015.

The ages of the rhyolite fields are poorly constrained but likely range from ~ 1.5 Ma for the Northern and Central Dome Fields (K/Ar method) (Luedke and Smith, 1983) to ~ 57 ka for the SDF (Ar/Ar method) (Heumann, 1999). The individual domes within the Northern and Central Dome Fields are within the range of uncertainty of the dating technique. However, Heumann (1999) reports 57 ± 8 ka for China Hat and North Dome, and 75 ± 6 ka for China Cap from sanidine Ar/Ar analyses, and indicates that uncertainties in the Ar/Ar data indicates a minimum difference in age of 3 ka. However, phenocryst assemblages and bulk geochemical analyses of China Hat and China Cap are indistinguishable, while the Northern Dome Field and SDF have significant differences (Ford, 2005). Basalts have been suggested to both pre- and postdate the rhyolite domes based on overlapping relationships (Mansfield, 1927; Fiesinger et al., 1982), although McCurry et al. (2015) suggests that poorly exposed basalt blocks on the flank of the

dome are instead coarse ejected debris rather than onlap of basaltic lava flows. They suggest the rhyolite domes are younger than the immediately adjacent basalt.

The rhyolite eruptive sequence for the lava domes began with phreatomagmatic explosive volcanism, and the development of maars and tuff cones. The best exposures of the tephra deposits are in a quarry on the northern end of China Hat. This tephra deposit consists of both pyroclastic surge and fallout deposits (Ford, 2005; McCurry et al., 2015), containing blocks of rhyolite and basalt xenoliths up to 0.5 m (Figure 5).



Figure 5-
Tephra
deposit
underlying
the China Hat
lava dome.
Note large
pumice blocks
in deposit.
Outcrop ~5 m
tall.

The pyroclastic rhyolite is estimated to constitute less than a few percent of the total rhyolite erupted (McCurry et al., 2015). The textures of the effusive rhyolite flows that constitute most of the domes are massive to flow-banded, pumiceous to dense and glassy (Dayvault et al., 1984; Ford 2005). Alkali feldspar and quartz are common vapor-phase mineralization products lining fractures and vesicles (Ford, 2005). Dayvault et al. (1984) report trace amounts topaz of in some vesicles, which was confirmed by XrF analysis, although it is very rare.

Common phenocryst phases are quartz > sanidine > plagioclase > hornblende ≈ biotite > Fe-Ti oxides (magnetite > ilmenite) (Ford, 2005). Lochridge (2016) divided phenocryst phases into different populations based on textural characteristics, illustrating the diverse crystal cargo of autocrysts and antecrysts carried by the rhyolites. He interpreted this to represent different rhyolitic regions of the evolving magmatic system that mixed prior to the eruption of the rhyolite (Figure 6).

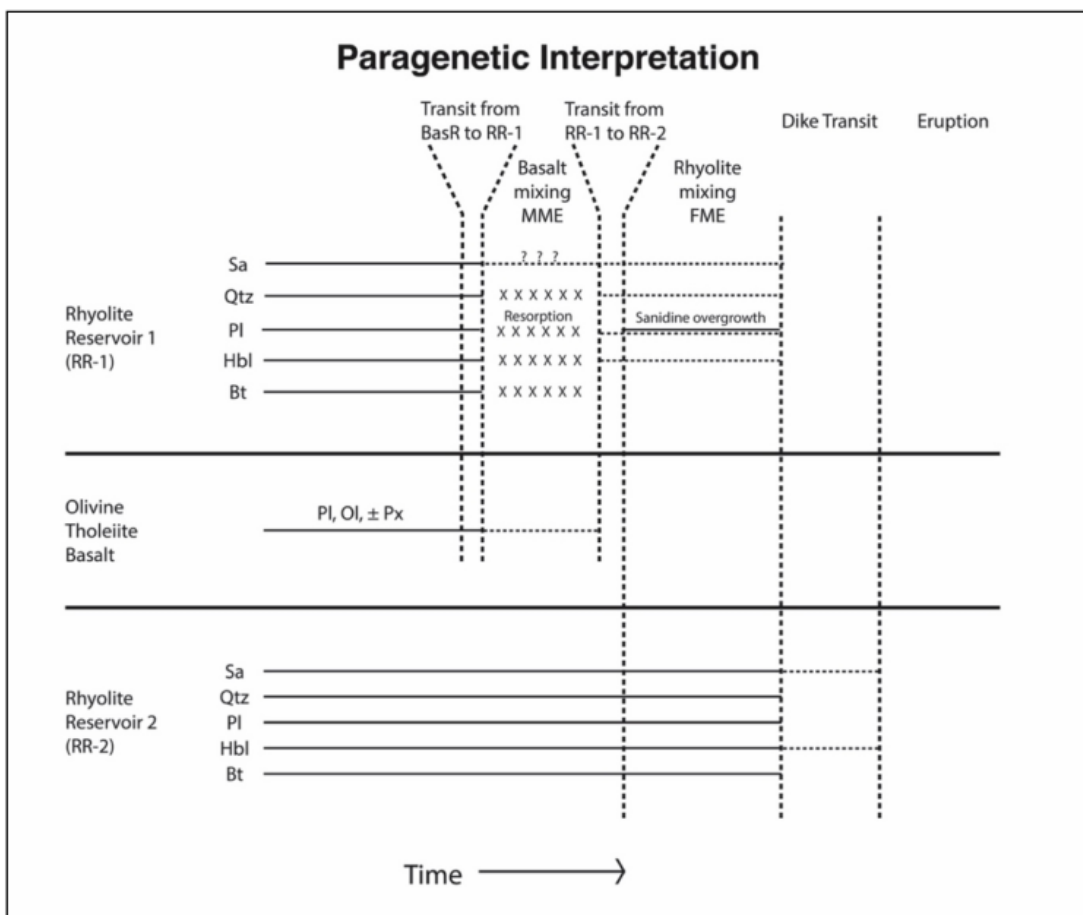


Figure 6 - Paragenetic interpretation based on phenocryst textural characteristics, demonstrating the diverse phenocryst assemblages in the rhyolite. From Lochridge (2016).

Al-in hornblende geobarometry applied to the rhyolites, based upon electron microprobe analyses of hornblende phenocrysts, indicated equilibration pressures of

3.45 ± 0.9 kbar, or about 13 km for the equilibration depth (Ford, 2005). Fe-Ti oxide geothermometry (Andersen et al., 1993), yielded a temperature of 758°C (Ford, 2005). This places the magma chamber near the location of the mid crustal sill that Peng and Humphreys (1998) proposed to underlie the ESRP.

Low-velocity geophysical anomalies located SE of the Eastern Snake River Plain have been interpreted as partially molten lower crust (Peng and Humphreys, 1998). This low-velocity zone projects under the BVF. This anomalous low-velocity zone is further supported by density and lithospheric strength models derived from gravity data (DeNosaquo et al., 2009), and from seismic data (Yuan et al., 2010), suggesting lower crustal flow from the ESRP to the southeast, supplying hot lower crustal material to the region under the BVF. This is also consistent with major, trace, and isotopic data for basalts suggesting that the volcanic rocks in the BVF are more similar to basalts along the Yellowstone/Snake River Plain than to basalts elsewhere in the Basin and Range (Ford, 2005; Pickett, 2004).

Low $^{87}\text{Sr}/^{86}\text{Sr}$ and high ϵNd isotopic values from SDF rhyolite analyses indicate a dominantly mantle-derived source for the rhyolites (Figure 7) (Ford, 2005). Ford (2005) modeled the isotopic evolution of the rhyolites using compositions of xenoliths for crustal composition, and indicated that the topaz rhyolites require 20 and 30 percent upper crustal assimilation to obtain the measured isotopic signature from a primitive basalt. He suggested the subsequent evolution of the magma is dominated by fractional-crystallization.

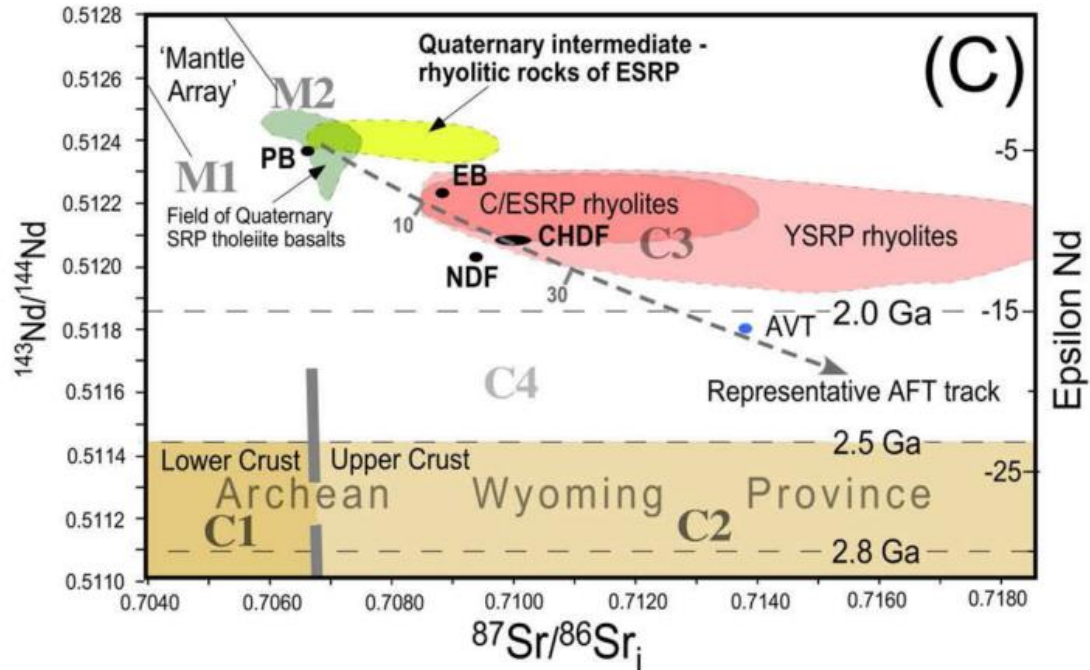


Figure 7- Nd, Sr isotopic plot illustrating the China Hat Dome Field (CHDF) rhyolites, in relation to primitive basalts (PB) and crustal regions. Ford (2005) indicates that 20-30% crustal assimilation of upper crustal material is required to create the isotopic ratios within the BVF rhyolites. From McCurry et al. (2015).

Preexisting model for the BVF

McCurry et al. (2015) presented an integrated petrotectonic model for the formation of the BVF, in which a deep, upwelling mantle plume impinging the base of the lithosphere spreads laterally under the BVF, which acted as a source of heat to the basal lithosphere of the ESRP and BVF. This hot plume induced melting in the lithospheric mantle, and the melt migrated upward to shallower reservoirs, such as the Moho as suggested by Peng and Humphreys (1998), as well as into the middle crust where crustal density declines rapidly (e.g. DeNosaquo et al., 2009). Most assimilation occurs in these deeper reservoirs, then melt continued to migrate upward to ~13 km

depth as suggested by Ford (2005), where additional storage and differentiation took place producing a pluton that likely had only a minimal volume of eruptible magma at any time (e.g. Bachmann et al., 2007), and the melt fraction fluctuated with incoming magma recharge. This process was hypothesized to produce highly evolved rhyolites, which were erupted to the surface in minor volumes (Figure 8).

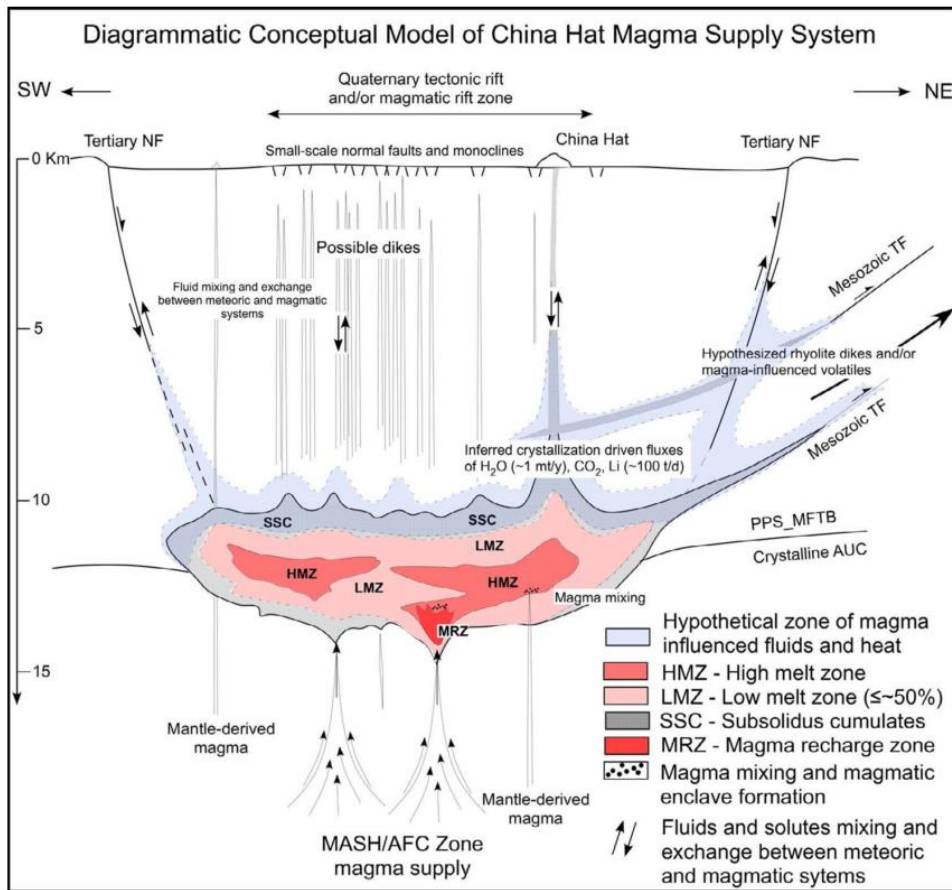


Figure 8- Conceptual model of McCurry et al. (2015).

Chapter 2: METHODS

This chapter discusses the methods used to test the hypotheses presented in the previous chapter.

Field methods

Thorough field examination of the China Hat and China Cap lava domes specifically focused on locating and documenting mafic enclaves was performed. Enclaves are very sparse in the lava domes, and constitute <<1% of the overall dome volume. Enclaves are more abundant in the China Cap dome than the China Hat dome. Within the China Hat dome, enclaves are much more abundant in the tephra deposit than in the lava dome.

Selected samples were then collected for petrologic and geochemical analysis. Rhyolites with enclaves were collected from the China Hat tephra quarry, the China Cap dome, and one from the China Hat dome (Figure 9; Table 1). Enclaves had not been noted in the China Hat dome prior to this study (cf. Ford, 2005; Lochridge, 2016), although Dayvault et al. (1984) noted a lithic inclusion of andesite in China Hat. A pumiceous rhyolite sample used for quartz separates was collected from the China Hat tephra quarry. Explosively-ejected material is preferred for melt inclusion work, as the quick cooling quenches the melt inclusions and allows less time for bubbles to form. Bubbles can increase the internal pressure of melt inclusions and cause leakage through capillaries (e.g. Lowenstern, 2003, 1995).

Sample Preparation Methods

Thin Sections

The method for thin section preparation followed that detailed in Ford (2005). In short, thin section billets of enclaves within the rhyolite were cut using a wet rock saw. Large enclaves were cut so that the enclave filled the majority of the thin section space, while smaller ones that would not fill the entire thin section space were cut so that they preserved the rhyolite-mafic contact. The billets were dried at 70°C for 12 hours before being sent to Wagner Petrographic for thin sections. Extra rock after cutting was used for X-ray Fluorescence (XrF) work. Petrographic observations were then conducted using a standard petrographic microscope.

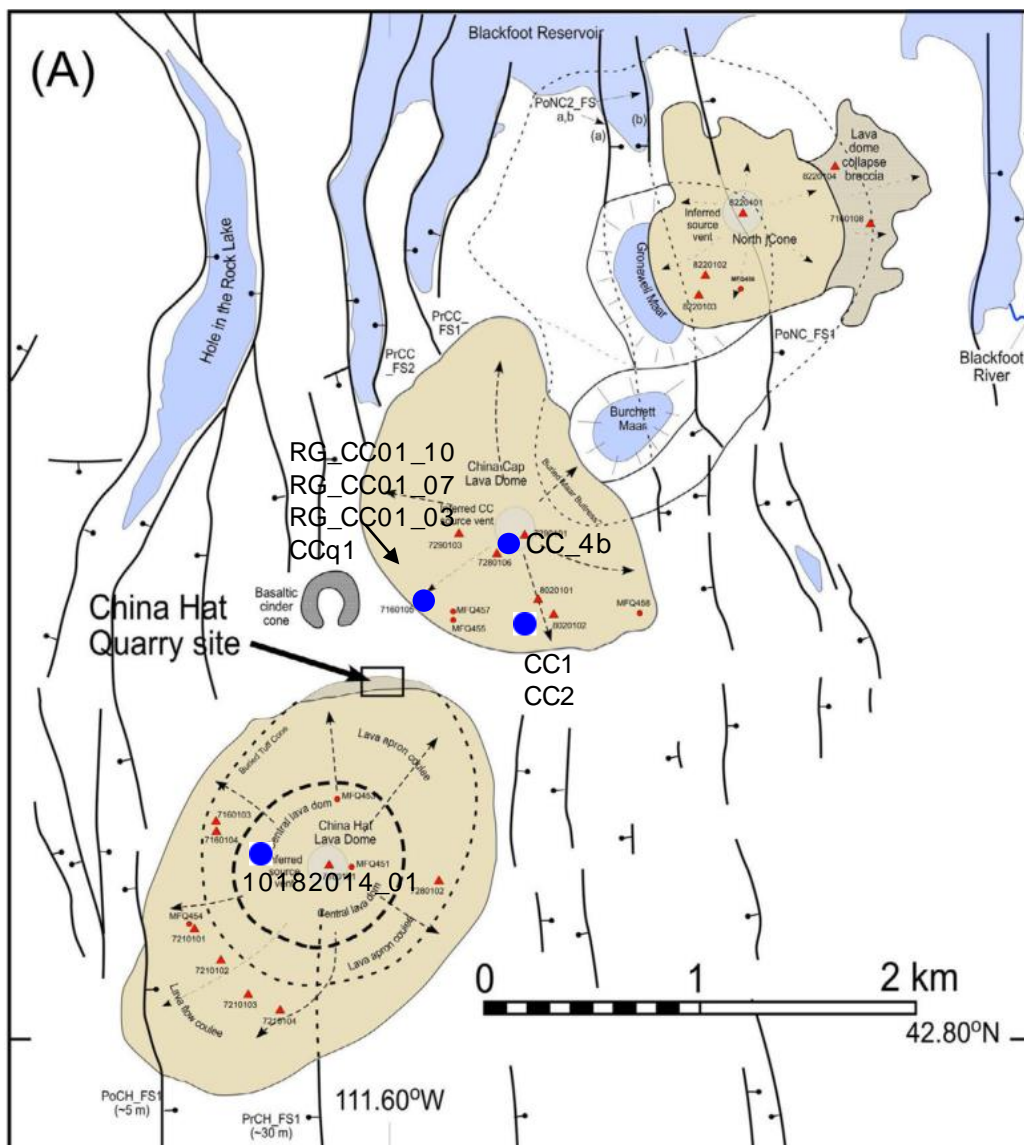


Figure 9- Blue dots indicate locations of enclaves collected from the southern-dome field. Also note the China Hat quarry site location where quartz phenocrysts were collected for ion microprobe analysis. Modified from McCurry et al. (2015). Lat/long of sample locations in Table 1.

XrF methods

XrF preparation followed the method of Ford (2005). Excess rhyolite was cut off of the enclaves using a rock saw. Then the samples were crushed to sub-centimeter size by hand using a steel plate and. Crushed samples were dried at 70°C overnight. The samples were then powdered to a ~300-mesh size (0.045 mm diameter) in a tungsten-carbide puck mill. Powder was stored in vials and labeled. All equipment was cleaned thoroughly between processing of each sample. The powdered samples were then sent to Dr. Eric Christiansen at Brigham Young University for XrF analysis.

<u>Sample</u>	<u>Latitude</u>	<u>Longitude</u>
CC1; CC2	42.818211	-111.591019
CC4	42.821277	-111.593322
RG_CC01_10; RG_CC01_07 RG_CC01_03; CCq1	42.819097	-111.599889
10182014_01 (China Hat enclave)	42.807939	-111.604167
RG071316-05 (Rhyolite for melt inclusions)	42.815015	-111.603898

Melt inclusion preparation methods

For melt inclusion work in quartz phenocrysts, a pumiceous sample from the China Hat quarry was crushed by hand using a steel plate and hammer to less than ~1cm. The crushed sample was passed through a 1.18 mm sieve, with the larger pieces being re-crushed on the steel plate. The fraction that made it through the 1.18 mm

sieve was then run through a 0.212 mm sieve, while the fraction less than 0.212 mm was discarded. This process was repeated until ~1 kg of sample was in the size range of 1.18 – 0.212 mm, which was within the range of quartz sizes documented previously in the rhyolite (Lochridge, 2016).

The glass and crystals from the sample were then separated using heavy liquids. Tetrabromoethylene was poured into a separatory funnel, along with ~30 g of crushed sample. Acetone was added and stirred into the mixture until the crystals sank while the glass remained floating. The crystals and glass were then filtered out of the funnel separately and rinsed with acetone. This process was repeated for ~100 g of sample.

Quartz crystals were then picked out of the crystal separate and placed into mineral oil to allow for easy identification of melt inclusions, as mineral oil has a similar index of refraction as quartz (Lowenstern, personal communication, 2016). Quartz crystals were then taken to Lowenstern's USGS lab in Menlo Park, CA; where small secondary crystallization was identified in many quartz crystals. ~50 crystals were chosen based on size, visible inclusions, and unbroken morphology, and were sent to Kurt Roggensack at Arizona State University for rehomogenization of the inclusions.

Dr. Kurt Roggensack at Arizona State University used a procedure similar to that of Sisson and Grove (1993) to rehomogenize the inclusions and to minimize the loss of highly volatile lithium and H₂O. The crystals were placed in a graphite capsule, which was heated 30° C per minute to 1010° C under 2 kbar of pressure. The sample was then held at 1010°C and 2 kb pressure for 10 minutes. The capsule was then cooled rapidly to quench the homogenized inclusions.

Ardalite 502 epoxy was mixed in the suggested proportions and placed into disposable syringes. PTFE coated washers with a 0.344-inch inner diameter were placed on scotch tape, and one crystal was placed in the center of each washer. The Ardalite epoxy was poured into each washer to create a flat disk with a crystal in the center of each. The washers were then placed in a tin foil boat and placed in an oven at 70°C for ~12 hours to dry the epoxy. The epoxy disks were then popped out of the washer, and the washers were reused for more samples.

The melt inclusions then had to be exposed on the surface of the sample to allow for SIMS analysis. 600 grit sandpaper and water was used first to grind the surface down to near the inclusion. Finer grit sandpapers were used until 1500 grit sandpaper exposed the surface of the inclusion. < 1 µm diamond polish on a Texmet C polishing pad was used for the final polish.

Microanalysis (EMP and SIMS) methods

The disks containing the melt inclusions were placed in acetone overnight and the crystals were removed from their earlier epoxy disks. The crystals placed into a larger epoxy disk using a similar method as outlined above. The crystals were placed polished side down onto tape, a brass ring was placed around them and lab technicians at Heidelberg University, Germany filled the disk with epoxy, so that all crystals were in one epoxy puck (Figure 10).

A Cameca SX51 Electron Microprobe (EMP) (under the direction and supervision of Dr. Hans-Peter Meyer at Heidelberg University, Germany) was used for major

element analyses of melt inclusions. The sample containing the quartz crystals was given a carbon coating to minimize charge buildup during analysis. A 20 μm beam size was used for most inclusions, and a 15 μm beam size used for smaller inclusions to minimize possible interference with quartz host. Melt inclusions were analyzed for: SiO_2 , TiO_2 , Al_2O_3 , FeO , MnO , MgO , CaO , Na_2O , and K_2O . Eleven standard glasses were used for element standardization, and element interference corrections were made to the melt inclusion measurements based on discrepancies between the accepted and measured standards.

After EMP analysis, the carbon coat was removed by the lab technicians who lightly polished it off. The sample was then given a gold coat using a sputtering machine that uses an Argon plasma in a vacuum to sputter a gold puck, which coats the sample in a thin gold coat. Then the sample was placed into a vacuum oven at 50°C for ~ 48 hours to prep it for the vacuum in the ion microprobe.

A Cameca IMS 3f Ion Microprobe was used for H_2O , Li, and B analyses under the direction and supervision of Dr. Axel Schmitt and Thomas Ludwig at Heidelberg University. An O_2 ion beam with a ~ 20 μm diameter and an intensity of 1 nA was used as the primary ion source to sputter the sample. The primary beam was run for 200 s before measurements began to pre-sputter the sample to remove absorbed hydrogen. After pre-sputtering, a 6- μm diameter aperture was placed in the way of the secondary ion beam, so that only ions from the inner 6 μm of sample hit by the primary beam were analyzed to avoid edge effects and any overlap the beam may have had with the quartz

host. Analyses for hydrogen, lithium, and boron were all run for 6 cycles for consistency, and internal reproducibility was calculated from the drift between samples.

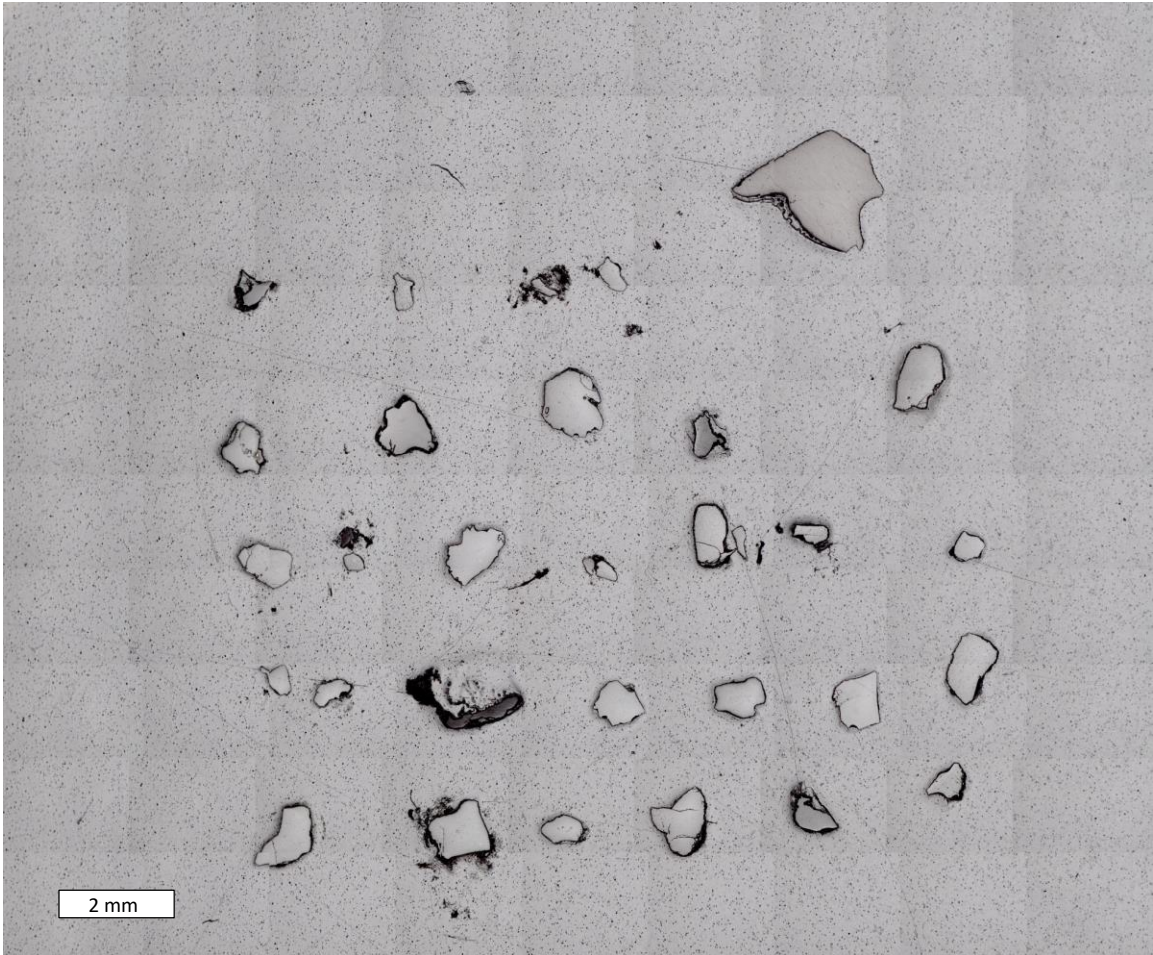


Figure 10- The quartz samples mounted in one epoxy disk. Reflected Light.

Chapter 3: RESULTS

Enclaves

Distribution and morphology

Here the term enclave is used as a non-genetic term to describe an inclusion of material different than that of the host rhyolite lava. Enclaves have been divided into genetic groups where different characteristics can be used to infer source of the enclaves (Didier and Barbarin, 1991; Table 2). Previous workers have documented mafic enclaves throughout the SDF (Fiesinger et al., 1982; Dayvault et al., 1984; Ford, 2005; Lochridge, 2016), but their genetic relationship to the topaz rhyolite has not been thoroughly explored.

Mafic enclaves are relatively abundant in the tephra deposits that underlie China Hat. Enclaves are also found in widely scattered groups in China Cap. Rare individual enclaves occur in China Cap, and one was found in China Hat. Locations of enclaves collected are given in Table 1. Rhyolite at outcrop to hand-sample scale contains 0-3% mafic enclaves. Individual enclaves range in diameter from <1 mm to ~14 cm (Figure 11). Swarms of enclaves range from ~10 cm to ~1 m across. The shapes of the enclaves vary from angular or ellipsoidal, to strung out, and boudin-like. Enclave margins vary from sharp rounded contacts with the surrounding rhyolite, to more diffuse, taking on a color between the dark mafic enclave and that of the rhyolite. Enclaves are black, to dark grey, to reddish grey. Some of the enclaves are sparsely vesicular, while others are dense. Many enclaves show embayed or crenulated margins. Enclave textures from the SDF are shown in Figure 11.

Term	Nature	Contact	Shape	Ovoid
Xenoliths Enclave	Piece of country rock	Sharp	Angular	Contact-metamorphic texture and minerals
Xenocrysts Enclave	Isolated foreign crystal	Sharp	Globular	Corrosion reactional aureole
Mafic Magmatic Enclave (MME)	Blob of coeval magma	Mostly sharp	Ovoid or Ellipsoid	Fine-grained igneous texture (But not always microgranular)
Cumulate Enclave (Autolith)	Disrupted cumulate	Mostly gradual	Ovoid	Large-grained cumulate texture
Felsic Microgranular Enclave	Disrupted fine-grain margin	Sharp or granular	Ovoid or Ellipsoid	Fine-grained igneous texture

Table 2- List and descriptions of enclaves found in igneous rocks. Most relevant to this study will be xenoliths, xenocrysts, and mafic magmatic enclaves. Modified from Ganske 2006, after from Didier and Barbarin, 1991.

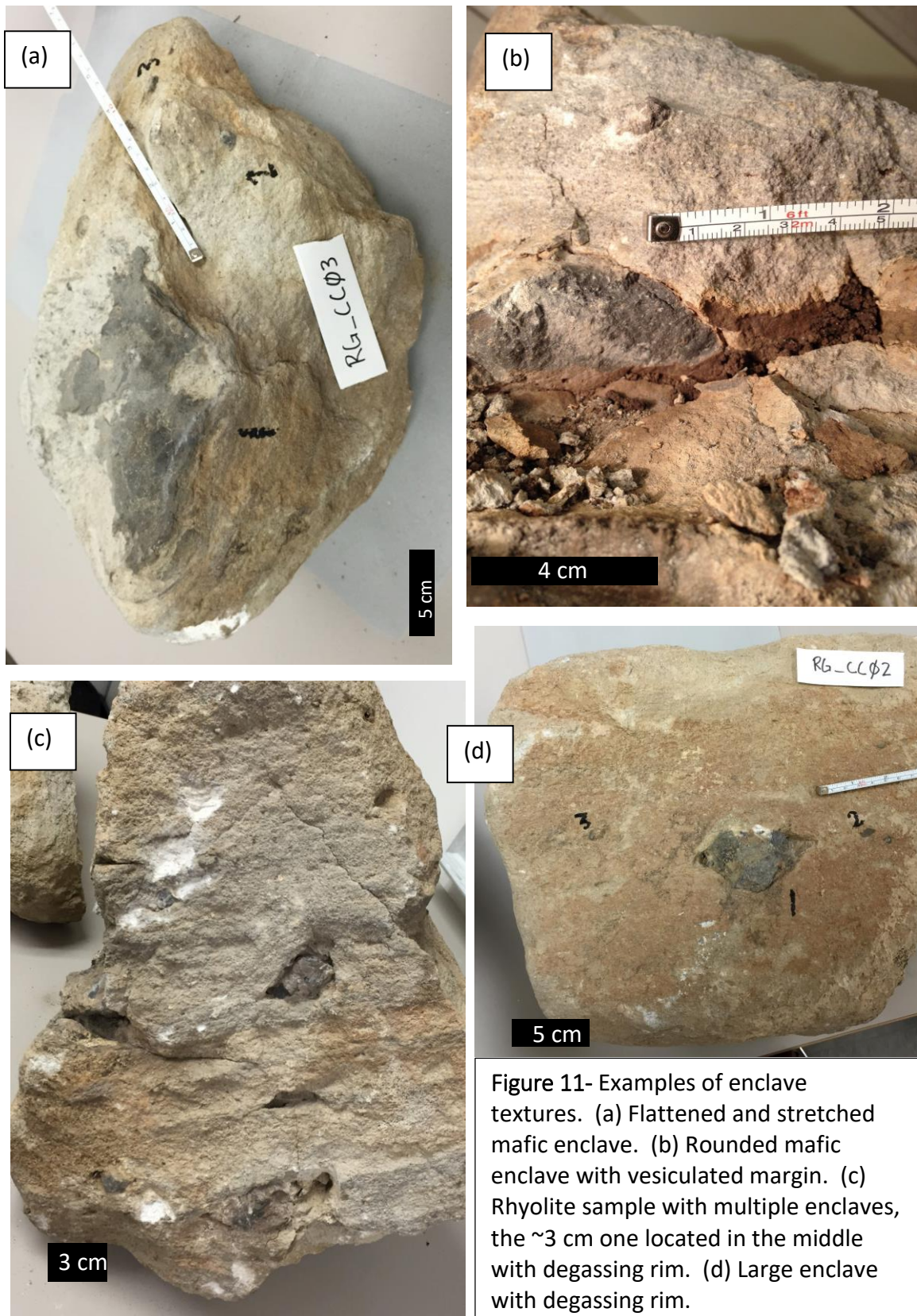


Figure 11- Examples of enclave textures. (a) Flattened and stretched mafic enclave. (b) Rounded mafic enclave with vesiculated margin. (c) Rhyolite sample with multiple enclaves, the ~3 cm one located in the middle with degassing rim. (d) Large enclave with degassing rim.

Petrographic features

Six enclave samples were studied in thin section. All of these enclaves contain sparse subhedral to euhedral plagioclase and olivine phenocrysts up to 1 mm in size. Stellate textures are common in both the plagioclase and olivine, which can form large glomerocrysts (Figure 12). Plagioclase crystals are commonly zoned with rounded, anhedral, resorbed cores (Figure 13), but often display euhedral rims. The mafic enclaves and the basalts of the BVF are similar in this olivine/plagioclase-dominated mineralogy, which is also similar to that of basalts of the ESRP (Pickett, 2004). However, one euhedral clinopyroxene phenocryst with a rounded, anhedral, resorbed core was found in sample CC_2 (Figure 14); Dayvault et al. (1984) also describes pyroxene bearing mafic “inclusions” in some of the lava domes. Interestingly, pyroxene does not occur as a autocryst phase in BVF basalts, nor in basalts of the ESRP (Pickett, 2004; Leeman, 1982).

Enclave/rhyolite contacts vary from < 1 mm to ~4 mm in thickness. Contact zones have a color index between that of the rhyolite and enclave. The contact zones also contain crystal phases that occur in both the enclave and rhyolite, and have fewer microlites than the enclaves (Figure 16). Ocellar quartz crystals in these zones are mantled by pyroxene reaction rims (Figure 15).

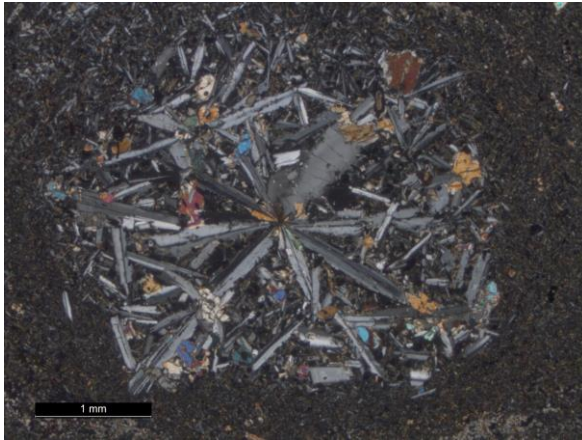


Figure 12- Stellate glomerocryst of plagioclase and olivine phenocrysts. Sample CC_01, crossed polars.

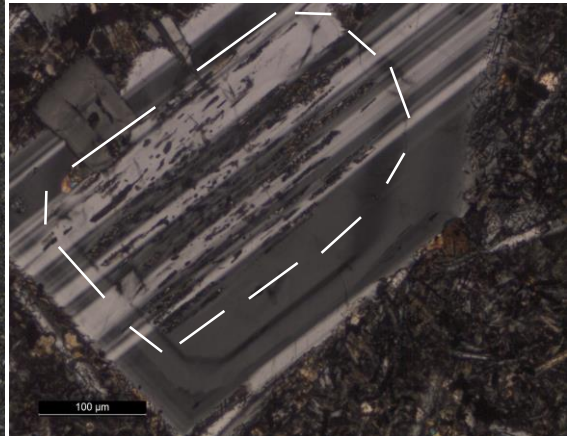


Figure 13- Zoned plagioclase phenocryst with resorbed core (outlined in white) and euhedral rim. Crossed polars, sample CC_2.



Figure 14- Clinopyroxene phenocryst in sample CC_2. Clinopyroxene does not occur as an autocryst in basalts of the ESRP nor the BVF. Crossed polars.

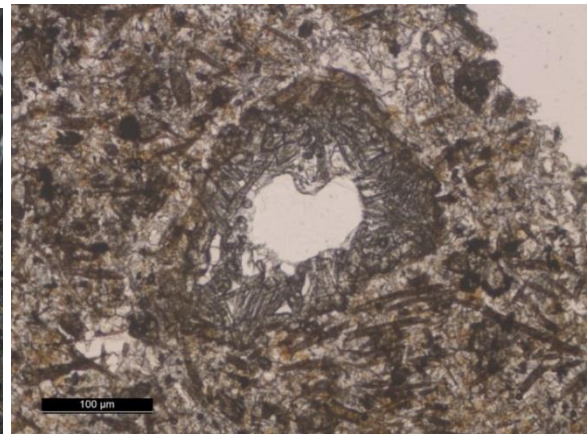


Figure 15- Ocellar quartz crystal mantled by pyroxene in sample CC_01_10. Plane light.

Bulk geochemistry

The normalized anhydrous XrF results of seven samples are given in Table 3. The mafic enclaves can be classified as medium to high-K basalts, basaltic andesites, andesites, and dacites using a total alkali-silica (TAS) diagram of Le Bas et al. (1986) (Figure 16). Element covariation trends are strikingly linear, with low R^2 values, for both major and trace elements.



Figure 16- Mixing zone (red line) between rhyolite (right) and mafic enclave (left). Note the zone has fewer microlites, and contains both olivine (green arrow) and kspars (blue arrow). Sample CCq1, crossed polars.

Table 3- Major and trace element whole-rock analyses from seven mafic enclaves analyzed via XrF. Data are normalized to anhydrous; major elements (yellow) are in weight percent, while trace elements (green) are in ppm. Analyses were conducted by Dr. Eric Christiansen, Brigham Young University.

		RG_CC01 _07	RG_CC01 _03	RG_CC q1	RG_CC _2	RG_CC _1	RG_CC _4b	RG_CC01_ 10
wt%	SiO2	49.92	50.03	54.25	54.71	55.51	58.50	64.33
	TiO2	2.50	2.50	2.12	2.05	1.89	1.67	1.15
	Al2O3	15.29	15.35	14.70	14.73	14.42	14.42	13.69
	Fe2O3	13.26	13.24	11.31	11.06	10.30	9.22	6.58
	MnO	0.18	0.19	0.17	0.16	0.15	0.14	0.11
	MgO	5.76	5.70	4.73	4.77	4.59	3.96	2.65
	CaO	8.64	8.61	7.58	7.16	7.83	6.06	4.54
	Na2O	2.46	2.49	2.76	2.80	2.70	2.92	3.25
	K2O	1.39	1.33	1.89	2.07	2.14	2.61	3.40
	P2O5	0.58	0.57	0.50	0.48	0.44	0.48	0.30
	Total	100.00	100.00	100.00	100.00	100.00	100.00	100.00
ppm	Ba	569	534	530	464	408	384	411
	Ce	53	55	58	56	55	53	50
	Cl	186	183	283	267	372	359	397
	Cr	69	72	45	48	43	38	25
	Cu	18	18	14	13	13	9	11
	F	2026	1083	2310	1316	1258	1639	4001
	Ga	21	21	20	21	20	21	21
	La	26	25	23	23	24	24	20
	Nb	29	30	37	37	39	45	56
	Nd	30	30	30	28	27	29	25
	Ni	51	51	37	38	35	33	21
	Pb	68	79	44	19	20	24	103
	Rb	82	83	138	138	153	187	271
	Sc	26	27	22	21	19	17	13
	Sm	7	7	6	7	6	7	6
	Sr	323	323	281	263	261	225	149
	Th	12	11	20	15	15	21	34
	U	3	4	8	7	8	11	15
	V	270	273	210	203	173	154	101
	Y	49	49	66	64	67	81	100
	Zn	117	124	107	99	93	90	82
	Zr	216	218	202	200	192	188	170

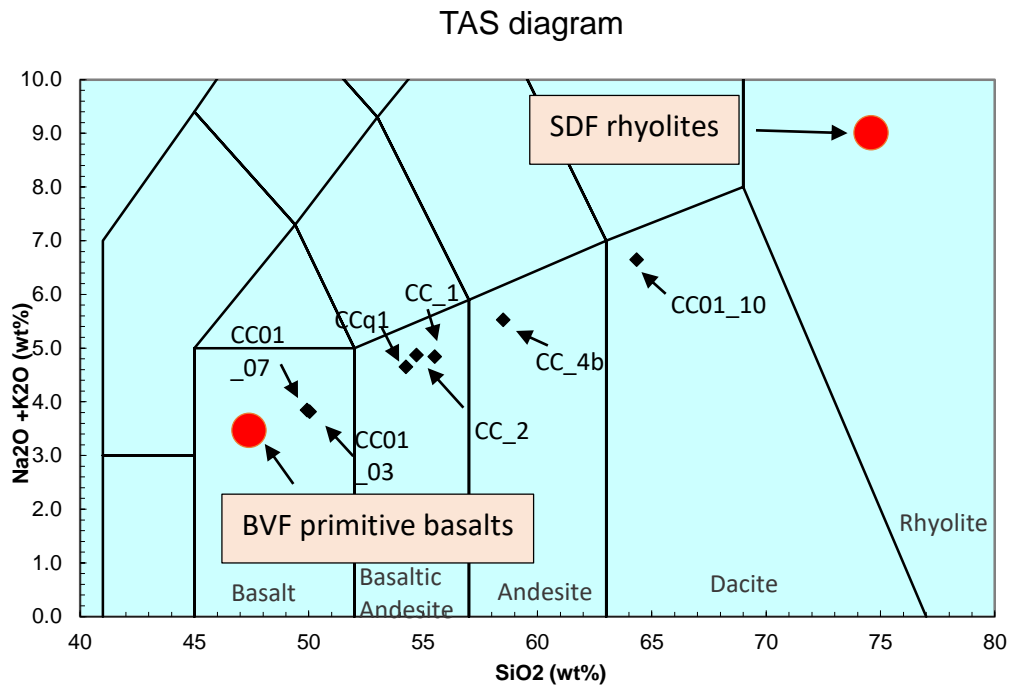


Figure 17- TAS diagram of Le Bas et al. (1986) with enclave analyses plotted from this study. Also plotted are BVF primitive basalts and SDF rhyolites from Picket (2004) and Ford (2005). Enclaves range from basalts to dacite. Lines represent compositional fields used for IUGS rock classification.

Melt inclusions

Morphology

Quartz-hosted melt inclusions are ~15-100 μm in diameter and have generally spherical to ellipsoidal geometries (Figure 18). Inclusions with apparent capillaries connecting them to the outside of the crystal were discarded prior to the homogenization process; however, several samples had evident capillaries after analysis (Samples 07 and 24; figure 19). These capillaries have previously been attributed to

leaking of inclusions, and therefore may not well-represent pre-eruptive melt volatile compositions (Lowenstern, 2003). Bubbles are present within about a third of the inclusions, while the rest appear visually homogeneous and free of microlites (e.g. Figure 18). Bubbles comprise between <1 - ~20 volume % of the inclusions.

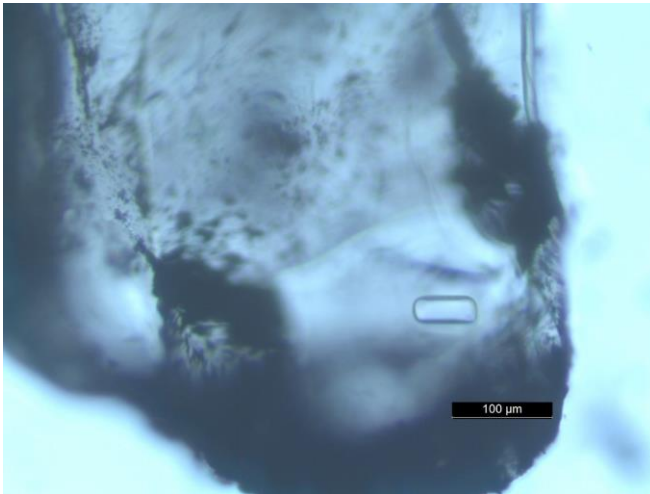


Figure 18- Elongate melt inclusion in a quartz phenocryst after homogenization.

EMP results

The EMP major element data are normalized to a 100 % anhydrous basis (Table 4). Some of the melt inclusions have silica percentages that are extremely high (~82%) for a rhyolite glass after normalizing to anhydrous. This unrealistically-high silica composition may be the result of either electron-beam overlap onto the quartz host, or from over-homogenization of the inclusions, leading to silica diffusion into the melt inclusion. To correct for this, the average SiO₂ content from melt inclusions under 79% SiO₂ (76.86 wt %) was used to normalize all melt inclusion data. This is slightly lower than that of measured matrix glass (77.72 wt %). A similar method was used by Hofstra et al. (2013) to normalize their data with measured Al₂O₃ content in matrix glass. The

rest of the major elements were adjusted by the multiplying the measured value to a normalization factor calculated by:

$$\frac{(100 - X_{Si}^*)}{SUM(X_M)}$$

Where X_{Si}^* is the adjusted silica percentage; and $SUM(X_M)$ is the sum of the measured major elements, excluding SiO_2 . The results of this normalization are shown in Table 5 and Figure 20. This normalization process reduces the range between the maximum and minimum values for most elements, and has the effect of reducing scatter on many the plots.

Additional normalized element plots are shown in Figure 21. Many variation diagrams form linear trends. Sample 15 is an outlier in most diagrams, which may be due to the small size of the inclusion ($\sim 15 \mu m$), however this outlier is not thoroughly explored in this thesis. FeO ranges from $\sim 0.6 - 1$ weight %. K_2O values are $\sim 4.9 - 4.1$ weight %. CaO values are $0.4 - 0.72$ weight % and have a negative correlation with K_2O (Figure 20b). Na_2O values are $4.4 - 3.7$ weight %, and have a slight negative correlation with Al_2O_3 values ($12.7 - 13.3$ wt %).

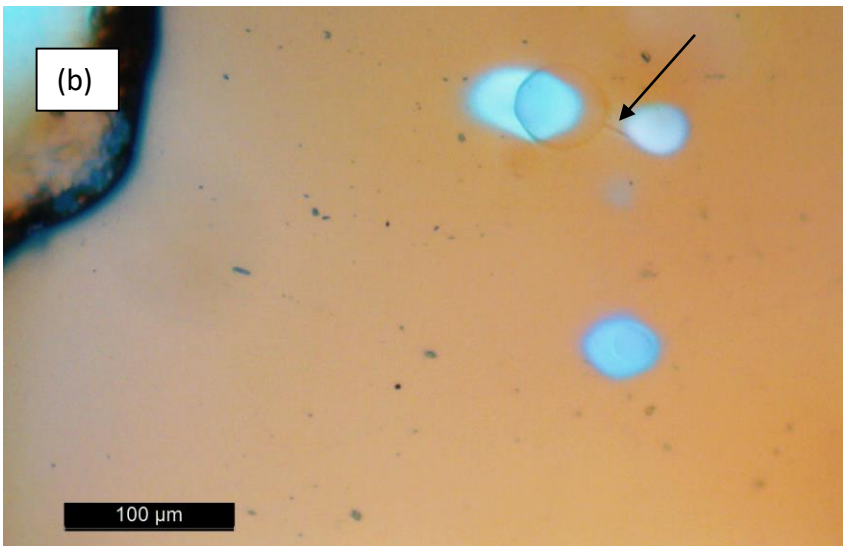
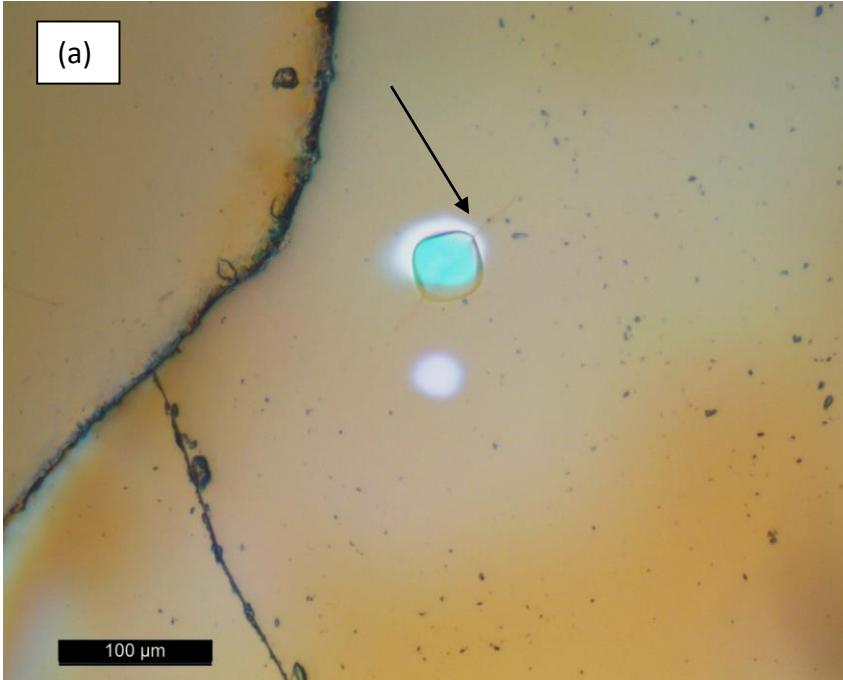


Figure 19- Samples with evident capillaries (indicated by arrows) after EMP and SIMS analyses. (a) Sample 7. (b) Sample 24. Combined reflected/transmitted plane light. Lighter spots are from the removal of the gold coating from the SIMS analyses. These lighter spots overlap the melt inclusions due to the processes of aligning the SIMS beam onto the inclusion.

Table 4- EMP major element analyses normalized to 100% on an anhydrous basis.											
Sample #	SiO2	TiO2	Al2O3	FeO	MnO	MgO	CaO	Na2O	K2O	Total Norm. Anhy.	Original Total
2	76.89	.06	13.22	.63	.07	.02	.69	4.20	4.21	100	95.37
2b	77.23	.07	12.52	.71	.07	.03	.63	3.75	4.17	100	94.60
4	80.51	.09	11.29	.72	.03	.02	.51	3.92	3.87	100	96.28
4b	80.40	.02	11.51	.76	.00	.03	.54	3.25	3.87	100	95.73
6	78.64	.02	13.62	1.03	.14	.01	.54	3.87	4.83	100	97.95
7	78.56	.02	11.55	.62	.02	.03	.54	3.75	3.86	100	94.37
7b	82.03	.07	9.99	.65	.01	.01	.37	3.38	3.47	100	95.35
8	78.67	.10	13.52	.86	.05	.02	.47	4.13	5.12	100	98.18
9	80.85	.02	10.98	.72	.03	.02	.50	3.61	3.74	100	95.82
10	77.58	.03	13.52	.99	.07	.02	.56	4.11	4.91	100	97.08
11	76.95	.11	13.07	.70	.03	.05	.69	4.21	4.30	100	95.47
11b	78.22	.10	13.61	1.01	.06	.04	.67	4.41	4.75	100	98.12
12	79.05	.03	9.60	.60	.01	.00	.41	3.12	3.55	100	91.91
13	79.91	.06	13.68	.94	.08	.02	.48	4.22	5.05	100	99.61
15	81.02	.05	12.19	.68	.09	.01	.59	1.89	3.51	100	95.41
16	81.52	.05	10.24	.57	.05	.01	.45	3.47	3.53	100	95.28
17	76.54	.09	12.43	.63	.08	.03	.60	3.99	3.83	100	93.68
18	77.10	.08	12.69	.70	.00	.04	.67	4.00	3.99	100	94.69
19	79.28	.05	13.12	.94	.00	.01	.52	4.31	4.18	100	97.67
20	81.25	.02	9.88	.56	.05	.02	.41	3.26	3.53	100	94.40
21	81.20	.08	10.08	.60	.09	.01	.45	3.29	3.42	100	94.63
23	79.02	.06	13.58	.91	.05	.02	.43	4.47	4.94	100	98.69
24	79.22	.06	11.08	.76	.03	.01	.51	3.41	3.75	100	94.26
25	76.61	.05	12.95	.81	.03	.03	.63	3.82	4.35	100	94.69
26	78.25	.07	12.98	.75	.08	.03	.60	4.28	4.34	100	96.69
27	76.55	.08	13.44	.85	.08	.02	.69	4.21	4.27	100	95.56
29	82.31	.05	10.06	.63	.00	.00	.48	3.29	3.51	100	95.70

Table 5- EMP data from table 4 are normalized to a SiO₂ content of 76.86 weight percent.

After Adjustment	SiO ₂	TiO ₂	Al ₂ O ₃	FeO	MnO	MgO	CaO	Na ₂ O	K ₂ O
02	76.86	0.06	13.24	0.63	0.07	0.02	0.69	4.21	4.21
04	76.86	0.10	12.77	0.82	0.04	0.02	0.58	4.44	4.38
06	76.86	0.02	13.10	0.99	0.13	0.01	0.52	3.73	4.64
07a	76.86	0.03	13.11	0.71	0.02	0.03	0.61	4.25	4.38
08	76.86	0.09	12.89	0.82	0.04	0.02	0.45	3.94	4.88
09	76.86	0.02	12.96	0.85	0.03	0.02	0.59	4.25	4.41
10	76.86	0.03	12.92	0.94	0.07	0.02	0.53	3.93	4.69
11a	76.86	0.11	13.06	0.70	0.03	0.05	0.69	4.21	4.30
11b	76.86	0.10	12.78	0.95	0.06	0.03	0.63	4.14	4.46
12	76.86	0.04	12.83	0.80	0.01	0.00	0.55	4.17	4.74
13	76.86	0.06	12.90	0.89	0.08	0.02	0.45	3.98	4.76
15	76.86	0.07	14.83	0.82	0.11	0.01	0.72	2.30	4.28
16	76.86	0.06	12.90	0.72	0.07	0.02	0.57	4.37	4.44
17	76.86	0.09	13.27	0.68	0.09	0.03	0.64	4.26	4.09
18	76.86	0.08	13.24	0.73	0.00	0.04	0.70	4.17	4.17
19	76.86	0.05	13.13	0.94	0.00	0.01	0.52	4.31	4.18
20	76.86	0.03	12.89	0.73	0.07	0.02	0.53	4.26	4.61
21	76.86	0.10	12.94	0.78	0.11	0.01	0.57	4.23	4.39
23	76.86	0.05	12.85	0.86	0.05	0.02	0.40	4.23	4.67
24	76.86	0.07	13.07	0.90	0.04	0.01	0.60	4.02	4.43
25	76.86	0.05	13.22	0.83	0.03	0.03	0.64	3.90	4.44
26	76.86	0.07	12.99	0.75	0.08	0.03	0.60	4.29	4.34
27	76.86	0.08	13.15	0.83	0.08	0.02	0.68	4.12	4.18
29	76.86	0.07	12.92	0.81	0.00	0.00	0.62	4.22	4.50

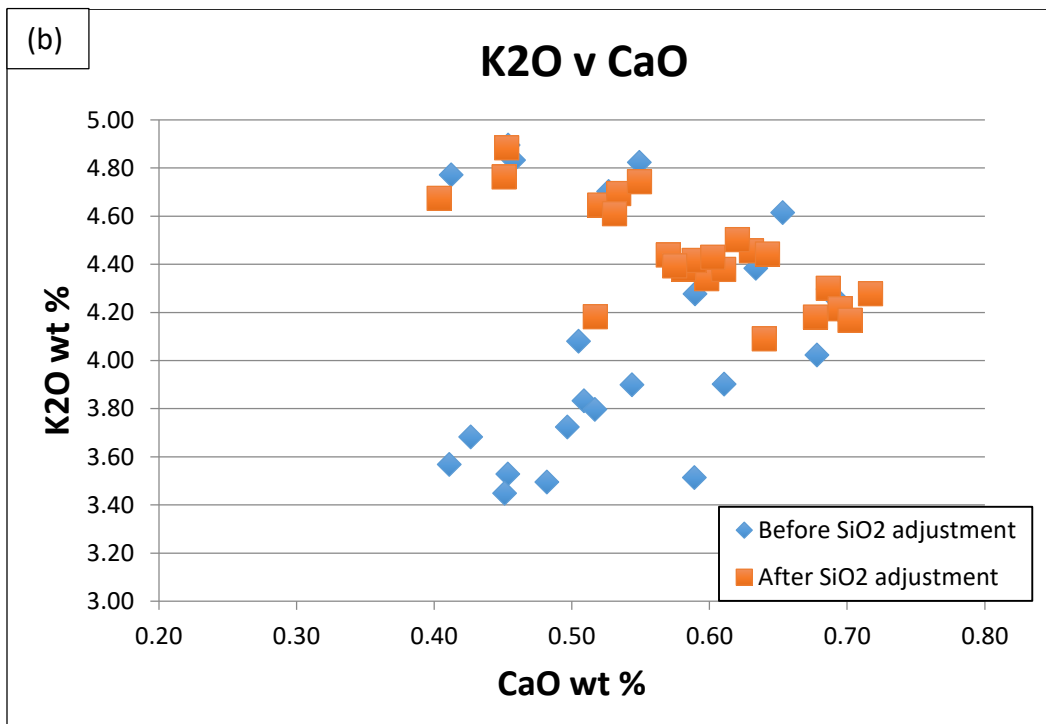
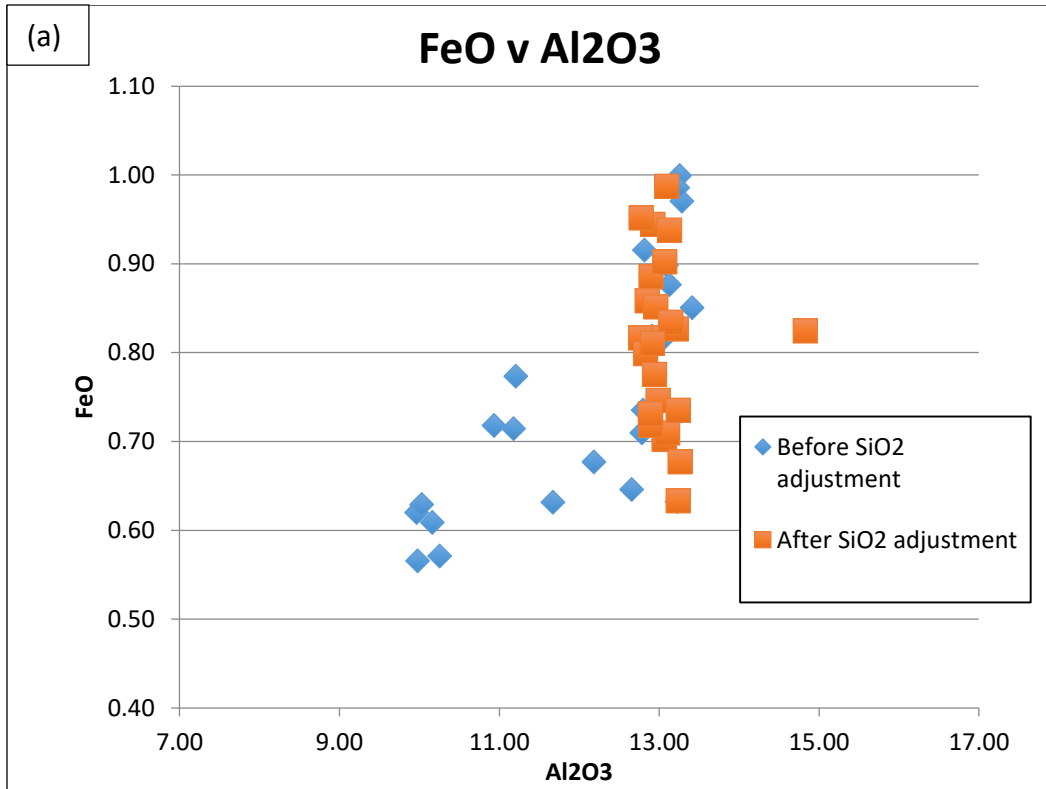
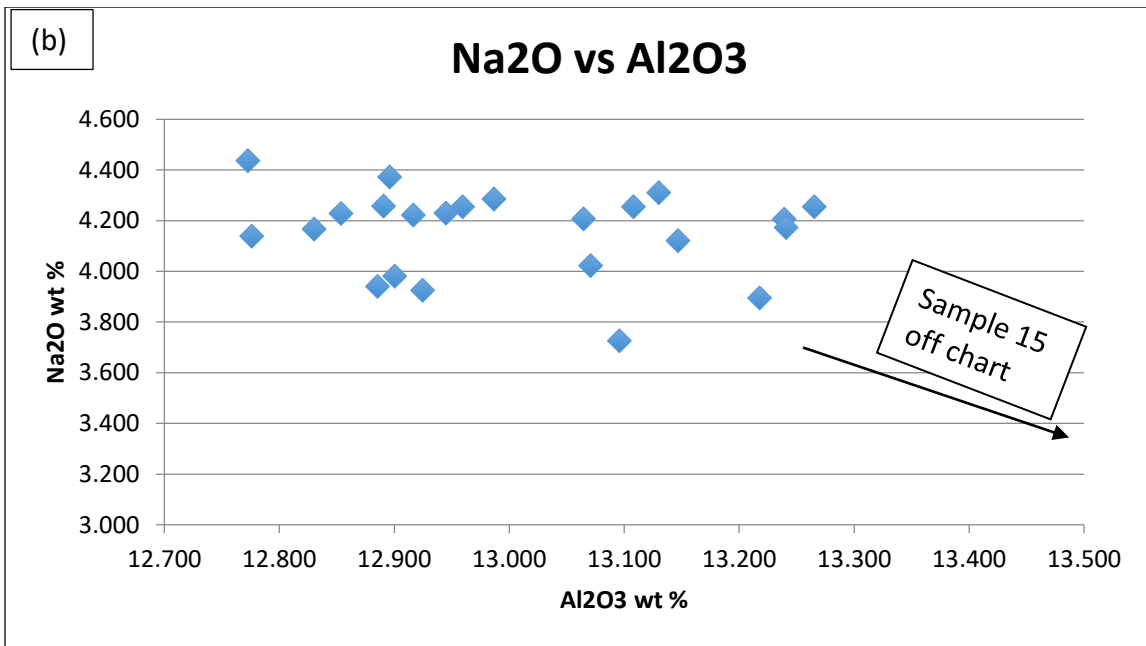
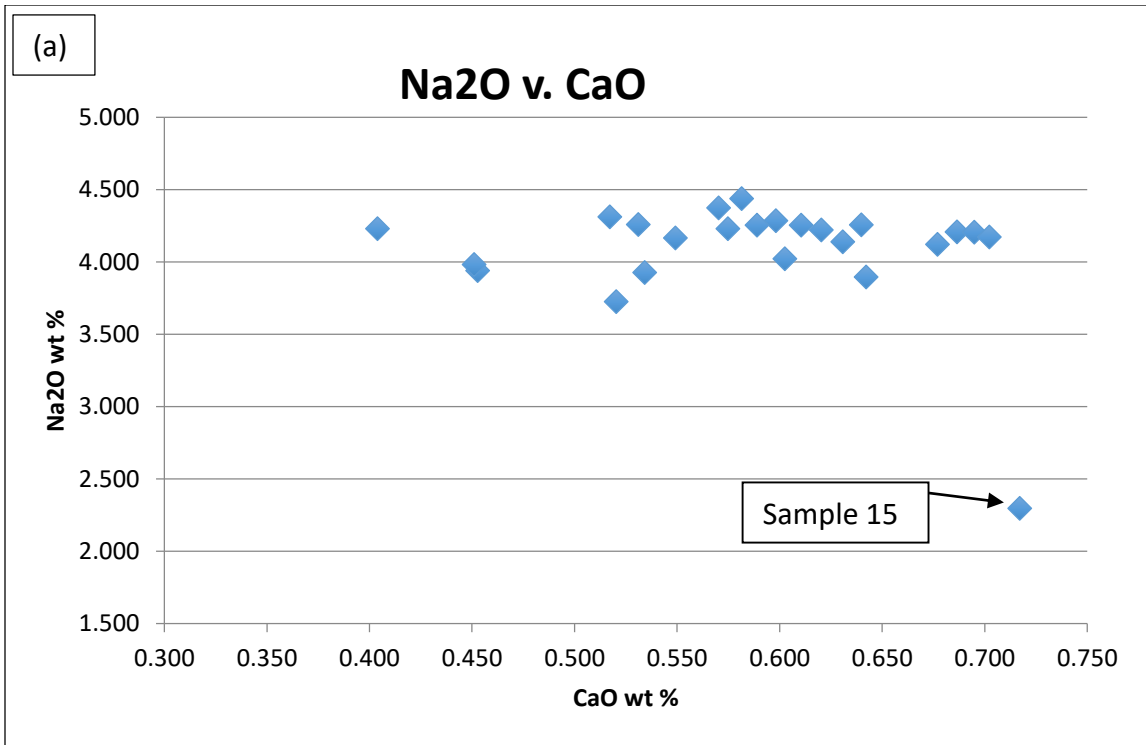


Figure 20- (a) FeO vs. Al₂O₃ of melt inclusions before and after adjusting to a normalized SiO₂ weight percentage of 76.86. (b) K₂O vs. CaO.



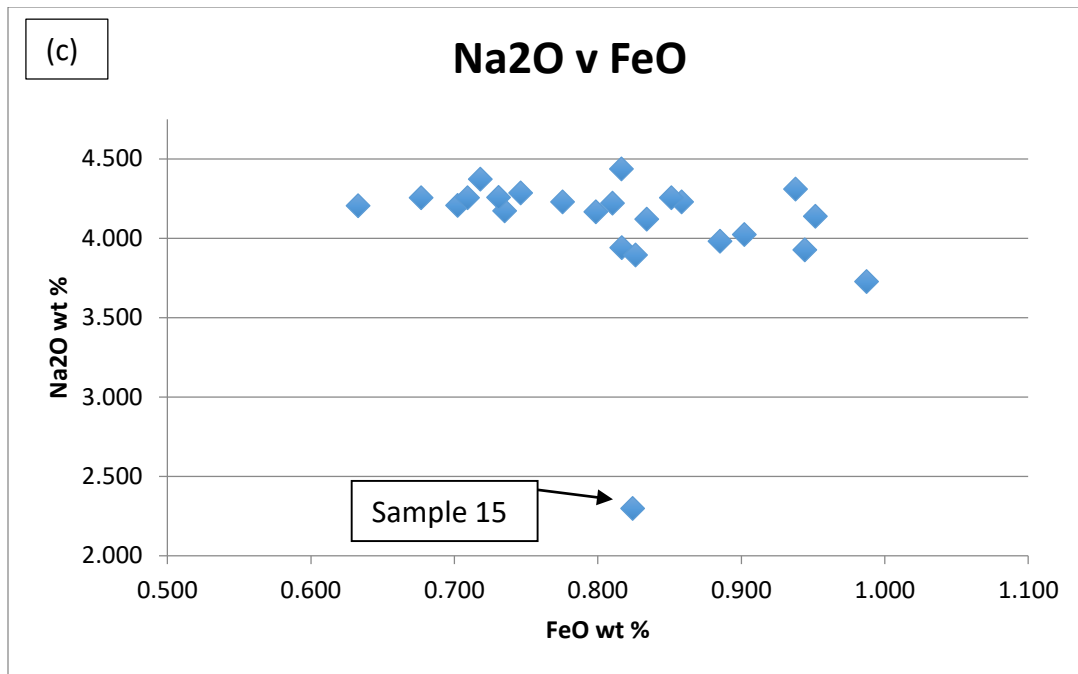


Figure 21- Silica-adjusted, normalized element variation diagrams from melt inclusions. (a) Na₂O vs. CaO (b) Na₂O vs. Al₂O₃. (c) CaO vs. MgO. The outlier, sample 15, is not plotted on (b).

SIMS results

Table 6 presents SIMS data of melt inclusions, in concentrations of H₂O (in weight percent), Li, and B (both in ppm). The internal precision of the measurements is indicated by the relative standard error and is calculated from the standard deviation of the six measurements per sample. The errors are reported to 2-sigma, and are recorded in weight percent for H₂O and ppm (ug/g) for Li and B. Lithium and boron are often used as geochemical tracers in geothermal exploration and related processes, and many geothermal fields have high lithium values associated with them (e.g. Hofstra et al., 2013).

If the high silica values of the melt inclusions are a result of overhomogenization (diffusion of silica from quartz host into the melt inclusion during the homogenization procedure) of the samples, then using measured SiO₂ values from the melt inclusions for calculation of volatiles should be done, as the volatile concentrations are calculated by the referencing to the SiO₂ concentration in the sample. However, if the high SiO₂

Table 6- H₂O, Li, and B concentrations and errors from melt inclusion analyses. RG-01-qtz* was an analysis of a quartz crystal. SRM612-3 was a standard glass used for calibration. RG-01 was not analyzed by EMP, so an average of the lower silica melt inclusions were used for the Si percentage (76.86 wt %).

ID	Concentrations			Standard Deviation (2σ)		
	H ₂ O	⁷ Li	¹¹ B	H ₂ O	⁷ Li	¹¹ B
RG-08	0.65	99.8	36.3	0.00	0.2	1.1
RG-01	3.00	50.6	26.7	0.01	0.9	0.6
RG-01-qtz*	0.00	0.3	0.0	0.00	0.1	0.0
RG-02	2.79	73.5	23.9	0.05	0.9	1.1
RG-04	2.47	68.8	21.3	0.01	0.4	0.8
SRM612-3	0.01	40.0	36.2	0.00	0.8	1.1
RG-06	0.06	51.9	30.3	0.00	0.7	0.8
RG-07a	4.56	134.3	25.3	0.01	0.7	0.8
RG-09	4.81	128.2	27.9	0.01	2.5	1.1
RG-10	0.59	68.7	27.4	0.01	0.5	0.7
RG-11a	2.89	61.3	22.3	0.01	0.5	0.6
RG-11b	1.12	83.8	18.3	0.01	0.4	0.7
RG-12	4.25	147.3	25.5	0.01	6.5	1.2
RG-13	0.20	100.4	82.9	0.01	1.0	4.3
RG-15	2.49	64.7	14.2	0.01	3.9	1.0
RG-16	4.24	59.9	24.1	0.01	0.5	0.8
RG-17	4.25	113.6	27.5	0.01	0.9	0.8
RG-18	2.99	55.1	18.6	0.02	0.7	0.8
RG-19	0.77	119.9	35.5	0.01	1.0	1.6
RG-19-2	0.67	120.3	35.7	0.00	0.4	2.2
RG-20	4.14	70.5	22.6	0.07	12.2	0.9
RG-21	4.59	89.4	22.3	0.10	10.6	0.8
RG-23	0.55	88.2	38.4	0.02	1.0	1.1
RG-24	4.36	162.9	20.9	0.07	25.2	0.4
RG-25	3.97	156.6	27.5	0.05	28.9	0.8
RG-26	2.14	61.8	29.9	0.01	4.1	1.2
RG-27	2.99	113.8	26.3	0.04	11.0	0.9
RG-29	4.44	82.5	23.5	0.08	12.3	1.1

values were from electron beam overlap with the quartz, then the adjusted SiO₂ values should be used, since they may more accurately reflect the actual SiO₂ concentrations of the inclusions. Regardless of the SiO₂ value used, it has a minimal effect on volatile concentration, and is nearly always within the margin of error. Here, the values are left unadjusted given that the source of the high silica values is unknown. Appendix 1 contains the Excel file where the effects of changing Si content can be calculated.

Bubbles in melt inclusions can form from several ways: (1) Leaking of the melt inclusion. Bubble formation and expansion during depressurization can increase the internal pressure in the inclusions, causing the melt and/or vapor phase to be forced out of the inclusion. This process can be assessed by visual examination of leakage structures from the melt inclusions, low H₂O values, and will constitute a high volume in the inclusion. (2) Incorporation of a volatile phase in the H₂O oversaturated melt. A vapor oversaturated melt will exsolve an H₂O-rich volatile phase, which may be captured during crystal growth. Captured volatile phases will also constitute a large volume of an inclusion. (3) Decompression of the melt upon cooling, resulting in a volume decrease and depressurization of the melt. This would cause a saturation of a volatile rich phase. These “shrinkage bubbles” typically only constitute a small percentage (0.1 – 5 vol. %) of the inclusion (Lowenstern, 1995, 2003).

The grouping of bubble-containing inclusions versus those without leads to curious trends on variation diagrams (Figure 22). Perhaps most immediately apparent is the grouping of H₂O values: one group between 4-5 wt%; one between 2-3 wt%; and a <1 wt% group. Bubble-containing inclusions entirely make up the lowest water group.

Boron has a high value of around 30 ppm for bubble-containing inclusions, with higher values for non-bubble containing inclusions. Lithium ranges in value from ~50 ppm to ~162 ppm, and is not correlated well with the other volatile concentrations (H₂O and B), nor with major elements. One thing to note is that sample RG-01 was not analyzed by EMP analyses due to an imperfection in the carbon coating, and is therefore not included in the charts that include SIMS data.

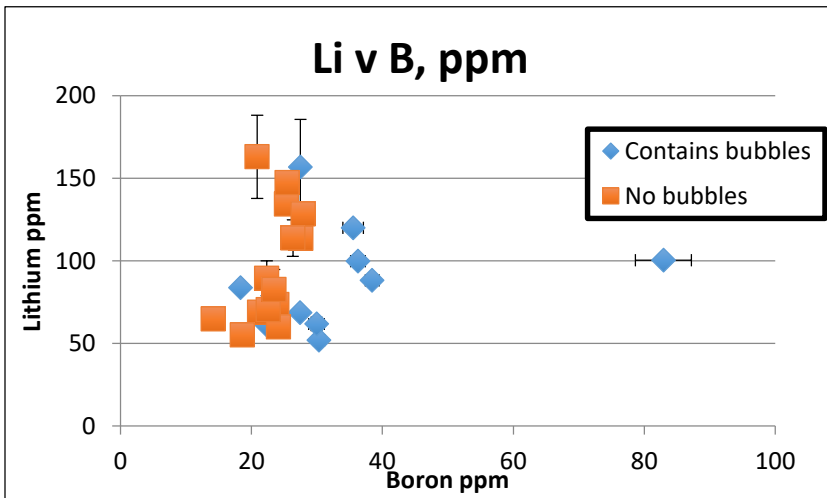
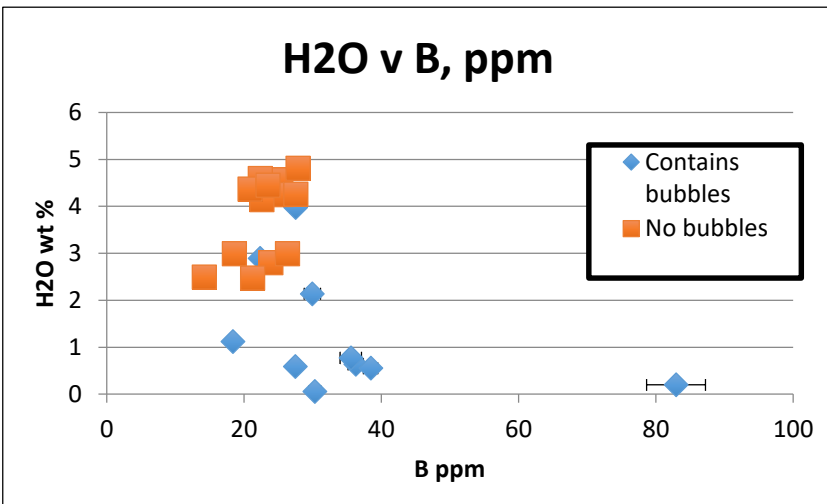
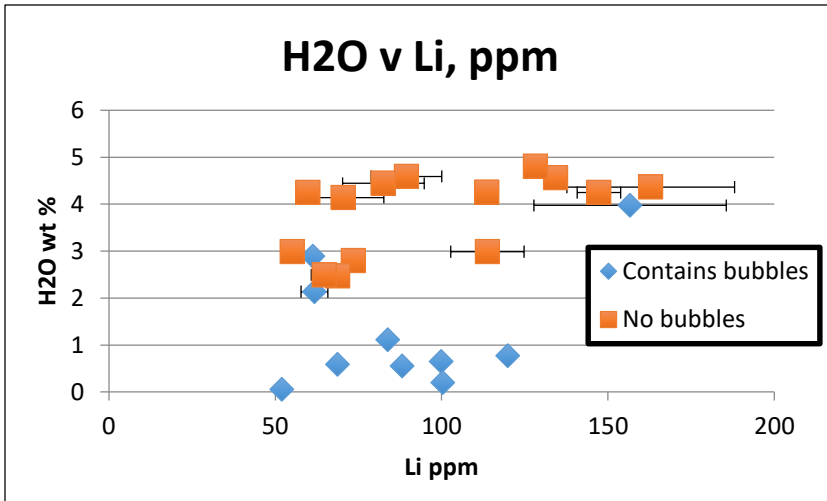


Figure 22- Volatile element plots from melt inclusions analyzed via SIMS. If error bars are not shown they are smaller than the symbol used.

Chapter 4: DISCUSSION/INTERPRETATIONS

This chapter begins with a slightly revised model of upper crustal structure in the BVF region. I then focus on interpretations made from the data collected from mafic enclaves and from melt inclusions contained within quartz phenocrysts. Furthermore, I address problems with previous hornblende barometry applied by a previous study, and apply a newer hornblende barometer. I attempt to unite this information with data from previous studies, in order to further the development of a comprehensive model for the development of these rhyolites, and the significance in context of topaz rhyolite petrogenesis. Finally, I briefly discuss what the implication of this work in the context of geothermal development in the BVF.

Preferred cross section model

The first issue that I address here is that previous models (e.g. McCurry et al., 2015; Welhan, 2016; Lochridge, 2016) used cross sections of Dixon (1982), which were based on wells and seismic data. However other cross sections (e.g. Royse et al., 1975; Yonkee and Weil, 2015) based on regional mapping, in addition to wells and seismic, show a more shallow thrust décollement than Dixon (1982). In this thesis I use the cross sections of Royse et al. (1975), which were created based on detailed surficial mapping as well as with local seismic and borehole data. These sections have better constraints on the subsurface architecture in the region of the BVF. Both Dixon's (1982) and Royce

et al.'s (1975) cross sections are better constrained closer to the foreland of the fold-thrust belt, east of the BVF.

One modification I make to the Royse (1975) cross section is the depth of the basin beneath China Hat. An exploratory well, the Hubbard #25-1, was drilled in 1981 to a depth of 2.36 km, ~2 km to the south of China Hat. The logs indicate the "Top of the Dinwoody Fm" at a depth of ~1.54 km, with everything above being sedimentary basin fill and basalts. The well bottomed out in limestone, which they interpret to be the Pennsylvanian Wells Formation (<http://geology.isu.edu/Geothermal/wells/api11-029-30001/HubbardANo25-1.Summary.Map.pdf>).

Enclave source

The information discussed in the previous chapters is here used to build an argument that the mafic enclaves represent an olivine tholeiitic basaltic magma, similar to that of olivine tholeiitic basalts of the surrounding BVF, that mixed with an evolved rhyolitic magma chamber prior to the eruption of rhyolite.

The observed diffuse, semi-hybridized boundaries between enclaves and rhyolites are interpreted to represent two magmas incompletely mixed prior to the eruption. The occurrence of phenocrysts from both sources in this zone clearly demonstrates a snapshot of this mixing process. In addition, quartz mantled by a clinopyroxene reaction rim within an enclave (Figure 15) is interpreted to signify physical mixing of phases between the separate liquids, and has been documented in many other cases of magma mixing (e.g. Vernon, 2004 and references therein). Had the

mafic enclaves been xenoliths of captured country rock material, this mixing boundary would not occur as a lower temperature rhyolite melt could not heat a basalt xenolith to its solidus (e.g. Bowen, 1928).

Furthermore, the linear trends between endmembers in the geochemical data suggest a mixing of basaltic magma with rhyolite. An important note is that the range in geochemical data does not represent different mafic magmas being intruded into the rhyolitic chamber. Instead, the range likely represents variable degrees of mixing given that XRF analyses yielded linear trends in chemistry. All the enclaves plot in a linear trend between basalts of the BVF, and the SDF rhyolites in most element covariation diagrams (Figure 22). Had this transitional zone been a diffusion dominated zone, non-linear covariation trends would be expected as elements diffuse at different rates (e.g. de Campos et al., 2011).

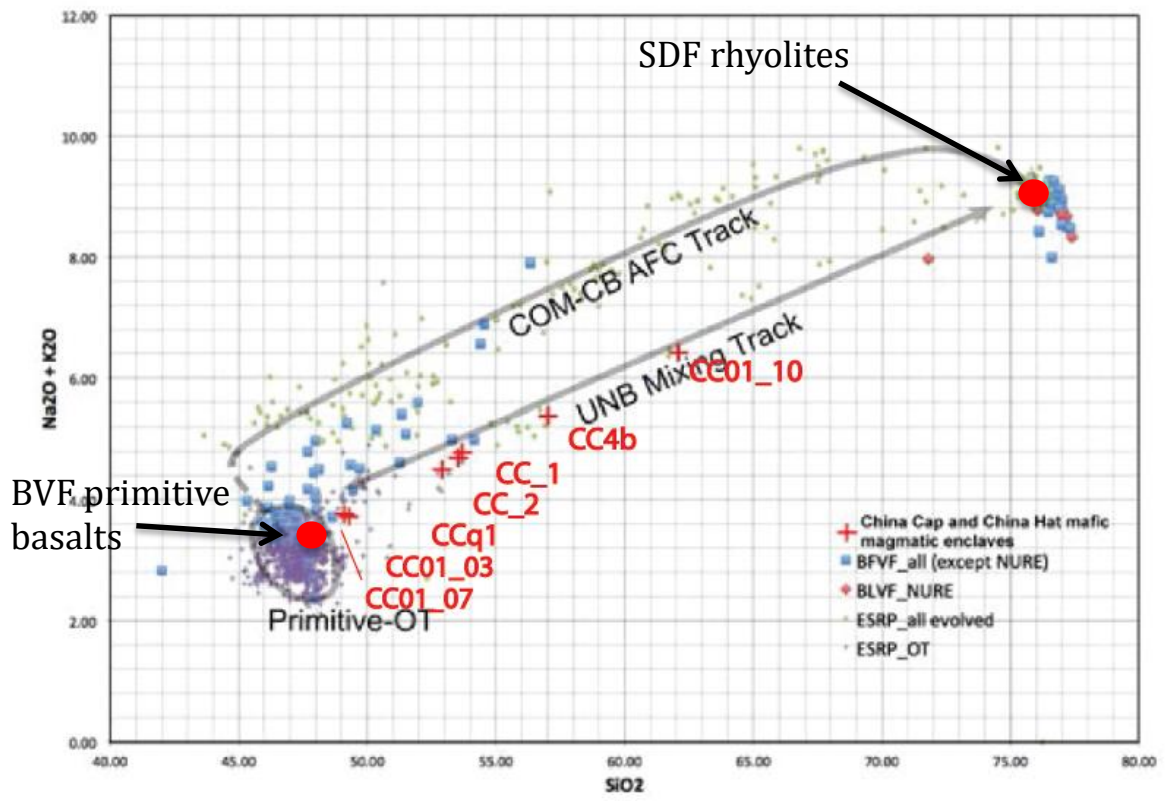


Figure 23- Enclave compositions plotted on TAS diagram, along with a primitive BVF basalt (from Pickett, 2004) and China Hat rhyolite (From Ford, 2005). Note that the enclaves form a linear trend between the two endmembers. Modified from McCurry et al. (2015), after McCurry et al. (2008).

The inferred primitive source identified here differs from some other Quaternary magmatic systems in the area. East Butte, a Quaternary high-silica rhyolite dome on the Eastern Snake River Plain, contains mafic magmatic enclaves that plot along curvilinear trends and therefore are not the products of simple mixing between primitive olivine tholeiitic basalts and the rhyolite (Ganske and McCurry, 2007). The mafic magmatic enclaves have evolved compositions, similar to that of the Cedar Butte-Craters of the Moon trend, which are suggested to have formed via fractional crystallization of a primitive basalt (McCurry et al., 2008). The enclaves in East Butte then represent a

more mafic magma chamber fractionally crystallizing, but mixed into the high-silica East Butte rhyolite prior to the eruption.

However, primitive magma mixing with rhyolitic magma chambers is also documented on the ESRP. Unnamed Butte, an intermediate to silicic volcano dated to 1.4 ± 0.028 Ma (Sanidine K-Ar) (Kuntz et al., 1994), occurs near other Quaternary rhyolites on the ESRP. Mafic enclaves, changes in bulk geochemistry, and Sr and Nd isotopic systematics demonstrates that Unnamed Butte is dominated by magma mixing between a primitive olivine tholeiitic basalt and rhyolite (McCurry et al., 2008).

So while it is apparent that some rhyolites in the region have contributions from highly fractionated mafic magma, the enclaves sampled in this thesis do not indicate evidence for such a process. Instead the enclaves are more similar to Unnamed Butte although robust phenocryst assemblages may indicate rhyolitic magma mixing (Lochridge, 2016). The role that the mafic enclaves have in a broader context of rhyolitic dynamic evolution is discussed later in this chapter.

Melt inclusion interpretations

The data obtained from melt inclusion analyses are used to infer the state of the pre-eruptive system, as discussed below.

Lithium and Boron concentrations in the melt inclusions do not correlate strongly with other variables. High boron values in the low-water, bubble-containing inclusions may represent contamination, as boron contamination occurs readily

(Schmitt, pers. comm., 2016), and the capillaries in the leaked inclusions may have permitted boron transfer into the inclusions.

Based upon the generally bubble free inclusions, and the gap between high H₂O contents, I interpret the two populations (~2.7 wt % and ~ 4.5 wt % H₂O) of H₂O concentrations in the melt inclusions represent different regions of melt with different volatile abundances. Furthermore, the low volume of bubbles in the inclusions in the groups likely represents shrinkage bubbles, although vapor-saturation is also possible.

The < 1 wt % H₂O group has low H₂O abundances, consists entirely of higher-volume bubble containing inclusions, and therefore I interpret this population to be a result of leaking and therefore to not be representative of pre-eruptive melt compositions.

These interpretations beg the question as to where these regions of melt are located within the crust, and how are they interacting and mixing to create the China Hat rhyolite from which the melt inclusions were collected from.

Lochridge (2016) suggested that different textural populations of quartz phenocrysts were derived from different zones of rhyolitic melt in the ~13 km deep consolidating pluton system. He interpreted these different zones of rhyolitic melt to indicate exchange of magma with each other prior to and/or during the eruptive sequence of the China Hat rhyolite, bringing together different crystal populations.

Chemical differences between melt inclusion populations further indicate different conditions of formation. Figure 24 illustrates higher CaO, and lower K₂O in the 2.7 wt % H₂O group compared to the 4.5 wt % group, with some overlap. The lower K₂O

component may indicate K_2O being partitioned into the volatile phase during a degassing event, however, a similar trend is not seen with Na_2O . CaO is higher in the 2.7 wt % group than the 4.5 wt % group, which would be consistent with K_2O loss into the volatile phase, as K has a higher diffusivity than Ca (e.g. Dingwell, 1990). However, I acknowledge that this is non-unique, and these trends could arise from other processes. Other major elements do not show significant trends. However, regardless of the source of the chemical variation between groups, I interpret it to represent different magma storage regions with different chemistries.

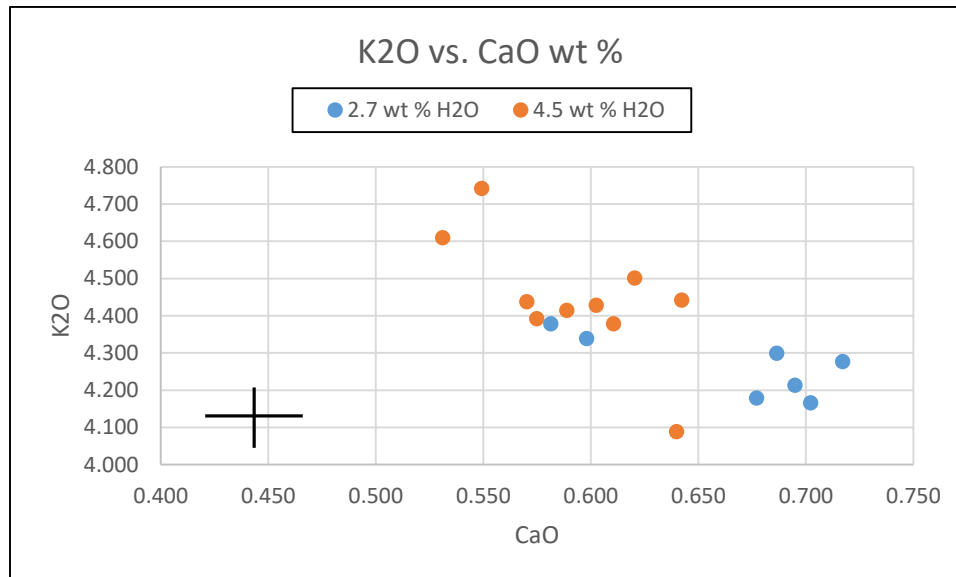


Figure 24- Plot illustrating lower K_2O and high CaO in the 2.7 wt % population of melt inclusions. Other elements do not show meaningful trends in chemistry. Black cross represents estimated precision of 4% RSD from the microprobe analyses.

MI normative mineral interpretations

The quartz stability field has been observed to expand relative to feldspars with increasing water contents under water-saturated conditions (e.g. Nekvasil & Burnham,

1987; Tuttle & Bowen, 1958); and the relative stability of feldspars is a function of water saturation in magmas (Student and Bodnar, 1996) (Figure 25). Using the average values of the two groups of melt inclusions, the CIPW norms were calculated (Table 7). The results indicate slightly higher normative quartz in the 2.7 wt % group, and higher normative feldspars in the 4.5 wt % group. Interestingly, the two groups plot very near the water undersaturated line of Student and Bodnar (1996), a possible indication of water undersaturation during melt inclusion encapsulation. Furthermore, the corresponding temperature on the plot (Slightly less than 780°C) is similar to the temperature obtained by Ford (2005) (~760°C).

Table 7- CIPW norm calculations from averages of different populations of melt inclusions.

	2.7 wt % H ₂ O	4.5 wt % H ₂ O
Quartz	35.70	33.84
Plagioclase	36.83	38.38
Orthoclase	25.18	26.24

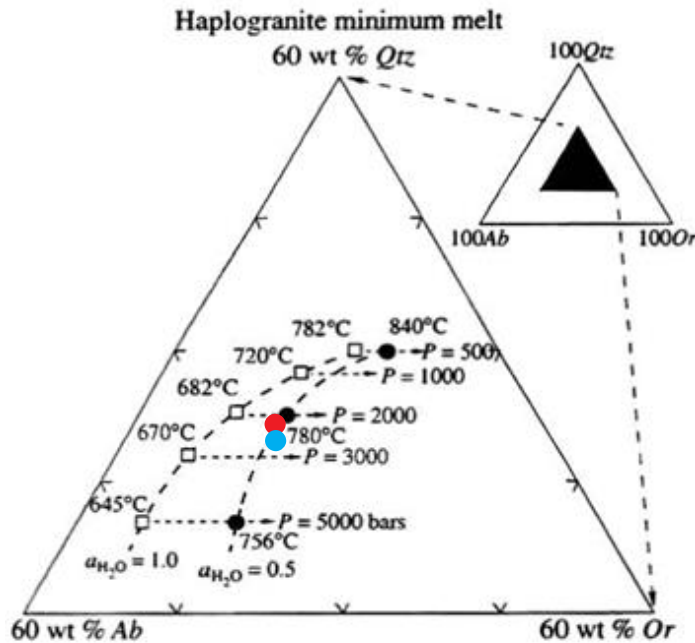


Figure 25- Stability relationships of phases with changing pressure and H₂O saturation. Note that one corner of the ternary represents 60 % components. Red circle is 2.7 wt % average. Blue circle is 4.5 wt % average. Qtz = quartz component, Ab = albite component, Or = orthoclase component. White squares are from a water-saturated system, black circles are data from a water-undersaturated system. The calculated norms lie along the undersaturated curve at a temperature slightly less than 780°C. Modified from Student and Bodnar (1996).

I interpret these differences in inclusion populations to represent evolution of the system at different volatile contents, and at H₂O undersaturated conditions. The relationship between the two populations is uncertain; however, since both populations plot along an H₂O undersaturated evolution surce (Figure 25) the above geochemical trends indicate the 2.7 weight percent group is not just the product of degassing of a 4.5 weight percent magma.

Vapor Saturation

The occurrence of bubbles in melt inclusions in the two higher H₂O content populations (Figure 22) is curious; if they formed as the result of depressurization and volatile loss, the inclusion should no longer record high water contents. The bubble could then then represent an inclusion only partially leaked before quenching, and shrinkage bubble, or it could represent the melt being oversaturated volatiles, exsolving a volatile phase, and subsequent capture of that phase by crystal growth (e.g. Lowenstern, 2003).

Careful observation of the higher H₂O melt inclusions that contain bubbles (Samples 11a, 26, and 25) indicated no apparent leakage structures or capillaries leading out of the melt inclusions. However, these observations were made post-sample preparation, so the third dimension cannot be analyzed for these leakage features. Therefore these bubbles are either shrinkage bubbles or they represent vapor saturation. I prefer the hypothesis that these are shrinkage bubbles, as argued above, however, if they are the the result of vapor saturation I make the following interpretations.

H₂O solubility in silicate melts is a function of temperature, pressure, and composition (e.g. Tuttle and Bowen, 1958; see Newman and Lowenstern, 2002 and references therein), and can be modeled based on experiments and/or thermodynamic data (e.g. Silver and Stolper, 1985). Newman and Lowenstern (2002) applied a thermodynamic model based largely off Silver and Stolper (1985) to produce a solubility

model for the melt-H₂O-CO₂ system (VolatileCalc) run in Microsoft Excel. VolatileCalc can calculate solubility at varying temperatures, pressures, and volatile contents.

However, CO₂ also plays a large role in volatile solubility in magmas (Silver and Stolper, 1985), and therefore must be accounted for as well. Without measuring CO₂ contents of the China Hat melt inclusions, assumptions have to be made about the CO₂ content of the system in order to obtain pressures, and therefore depths, of magma storage. However, by using a plausible range of CO₂ contents, interpretations are made about the magmatic system.

In the following interpretations, I assume that CO₂ contents of the melt inclusions are less than 1000 ppm. This is justified because: (1) 1000 ppm is at the very high end of measured CO₂ contents in rhyolitic melt inclusions from other studies (e.g. Lowenstern, 1994; Preece et al., 2014); (2) For a depressurizing system exsolving volatiles into the surroundings, CO₂ is preferentially exsolved into the melt relative to H₂O, resulting in rapid decrease in CO₂ content of the melt (Newman and Lowenstern, 2002)

Regardless of CO₂ concentration used (under 1000 ppm), pressures are less than the 3500 ± 400 bars (12.7-13.4 km depth) from hornblende barometry (Ford, 2005). A pressure vs. CO₂ solubility relationship was created using VolatileCalc for the two high H₂O content melt inclusion populations. At 4.5 weight percent H₂O, the pressure ranges from 1151-2505 bars depending on CO₂ content. Similarly, at 2.5 weight percent H₂O, the corresponding pressures are 456-1755 bars (Figure 26).

Using a crustal density of 2670 kg/m³ (Mabey and Oriel, 1970) the pressures then correspond to depths of 9.56-4.39, and 6.70-1.74 km, respectively. I use these ranges to make interpretations and expand upon previous models of the BVF later in this chapter.

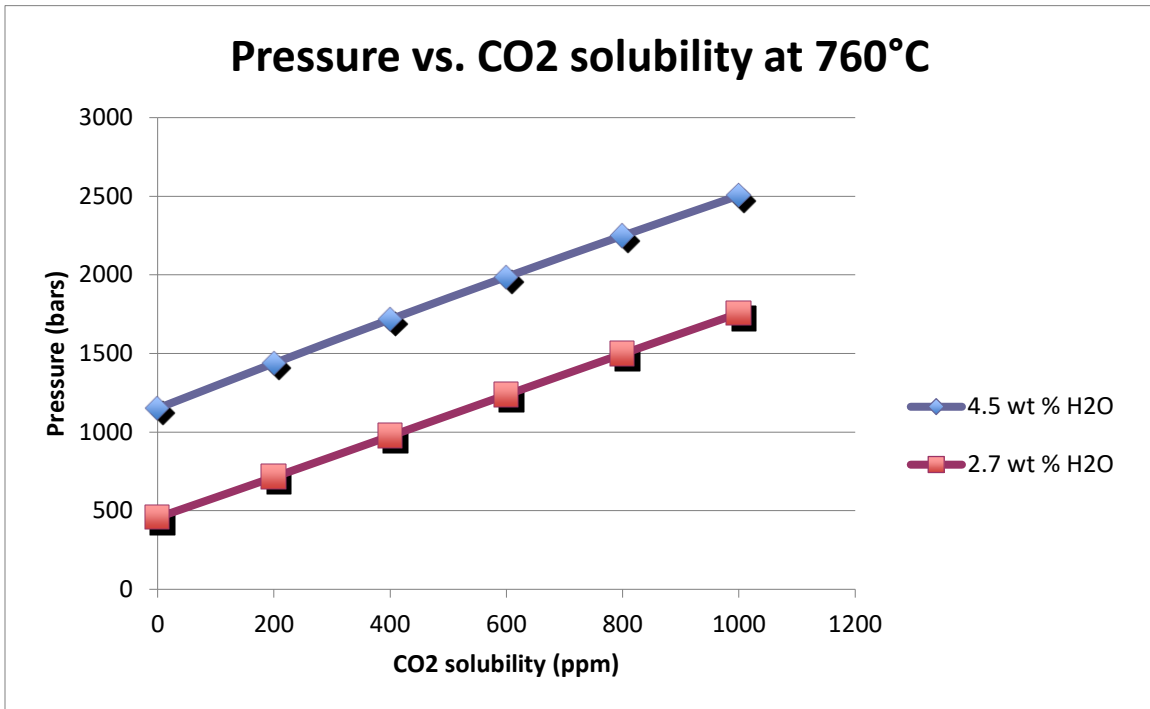


Figure 26- Plot of equilibration pressure vs. CO₂ solubility in rhyolitic melt, using the volatile solubility program VolatileCalc (Newman and Lowenstern, 2002). Regardless of CO₂ content assumed (<1000 ppm) pressures are less than pressures indicated by hornblende barometry. However, these estimations of pressure are only applicable if the assumption of volatile saturation is correct.

Amphibole barometers

Elemental partitioning in amphiboles shows significant potential to constrain depths and pressures of crystallization (e.g. Hammarstrom and Zen, 1986; Johnson and Rutherford, 1989; Ridolfi and Renzulli, 2012; Molina et al., 2015; Mutch et al., 2016).

Ford (2005) used the Johnson and Rutherford (1989) barometer contained within the

amphibole analysis software AMPHCAL (Yavuz, 1996) to constrain crystallization depths of the amphibole. Ford (2005) indicates a range in pressures of 3470 ± 410 bars, corresponding to a depth of 13 ± 0.4 km.

However, this depth was formulated from only using a pressure of 3500 bars, and the range of depths is the range obtained from using crustal densities of 2.67 and 2.8 g/cm³. This does not account for inherent uncertainties in the barometric model, nor the range of pressures obtained from hornblende analyses. Using his lowest value obtained from the model (3060 bars) and taking into account the estimated ± 500 bars precision (1σ) in the geobarometer (Johnson and Rutherford, 1989), corresponds with a minimum pressure of 2560 bars. Using a crustal density of 2.67 g/cm³, that results in a minimum depth of 9.81 km. Similarly, using a maximum pressure value of 4348 bars and a density of 2.67 g/cm³ a maximum depth of 16.7 km is obtained. While these results are much less precise than that suggested by Ford (2005), it more accurately represents the plausible range of depths of amphibole crystallization in the crust from the Johnson and Rutherford (1989) model.

A more recent barometer calibrated from experimental and measured natural data allows for a more precise determination of crystallization depth. Here I apply the method of Holland and Blundy (1994) to determine amphibole chemistry used on hornblende analyses from Ford (2005). The implementation of this new Al-in-hornblende barometer (Mutch et al., 2016) results in a pressure of 3.18 ± 0.51 kbar (1σ). This places a tighter constraint on pressure than the $3.45 \pm \sim 0.9$ kbar from the recalibration of Ford (2005). Assuming a crustal density of 2670 kg/m³, 3.18 ± 0.51 kbar

corresponds to 9.96-14.56 km depth (Table 8); which still encompasses the 13 km depth as suggested by Ford (2005).

Table 8- Recalculation of Johnson and Rutherford (1989) barometer using Ford (2005) amphibole analyses. These amphibole analyses are then applied to Mutch et al. (2016) barometer. All results to 1σ .		
	Johnson and Rutherford (1989) Recalculation of Ford (2005)	This study (using data from Ford (2005)) and method of Mutch et al. (2016)
Pressure (kbar)	3.45 ± 0.9	3.18 ± 0.51
Corresponding depth (km)	13.3 ± 3.5	12.18 ± 1.96

Model for the BVF

I use the information detailed above to create a model for the BVF (Figure 26), as outlined below.

The enclaves represent primitive mafic magma injection into the system prior to the eruption of the rhyolite. This mafic magma is similar to the surrounding basalts of the BVF and is sourced from the mantle with limited crustal storage. Although no constraints are made about the depth of magma mixing, I place the location of mixing to occur in the ~13 km depth magma reservoir of Ford (2004); which would be a lower density sub-solidus material the rising basalt would intercept.

This addition of heat and mass into the system drove interaction and mixing of distinct regions of rhyolitic melt, which is the source of the robust textural phenocryst assemblage (Lochridge, 2016). These distinct regions have different volatile contents

and slightly different major element compositions, indicating their unique evolution.

This addition of heat may have caused partial melting of the mostly solid magma reservoirs, which may act to enhance the enrichment in incompatible elements thought to be driven by extreme fractional crystallization (e.g. Ford, 2005; Lochridge, 2016; McCurry et al., 2015). Overpressurization from the addition of mafic melt may have been the driving force behind magma migration in the crust.

However, if the bubbles in the water-bearing melt inclusions represent volatile saturation, the melt inclusions could not represent crystallization of quartz at depth, as the measured water contents are not high enough to be oversaturated at 13 km. This then would necessitate a region (or regions) of shallower storage in the crust. This area of shallower storage is constrained to be ~9.5-1.7 km deep, regarding both populations inclusions. I place this reservoir at the boundary between Precambrian and Cambrian rock at about 9 km depth (Royse et al., 1975), although it should be noted that there is considerable uncertainty about the depth (and existence) of this magma reservoir. Furthermore, the cross sections become less precise with depth, and the deep structure is not well constrained.

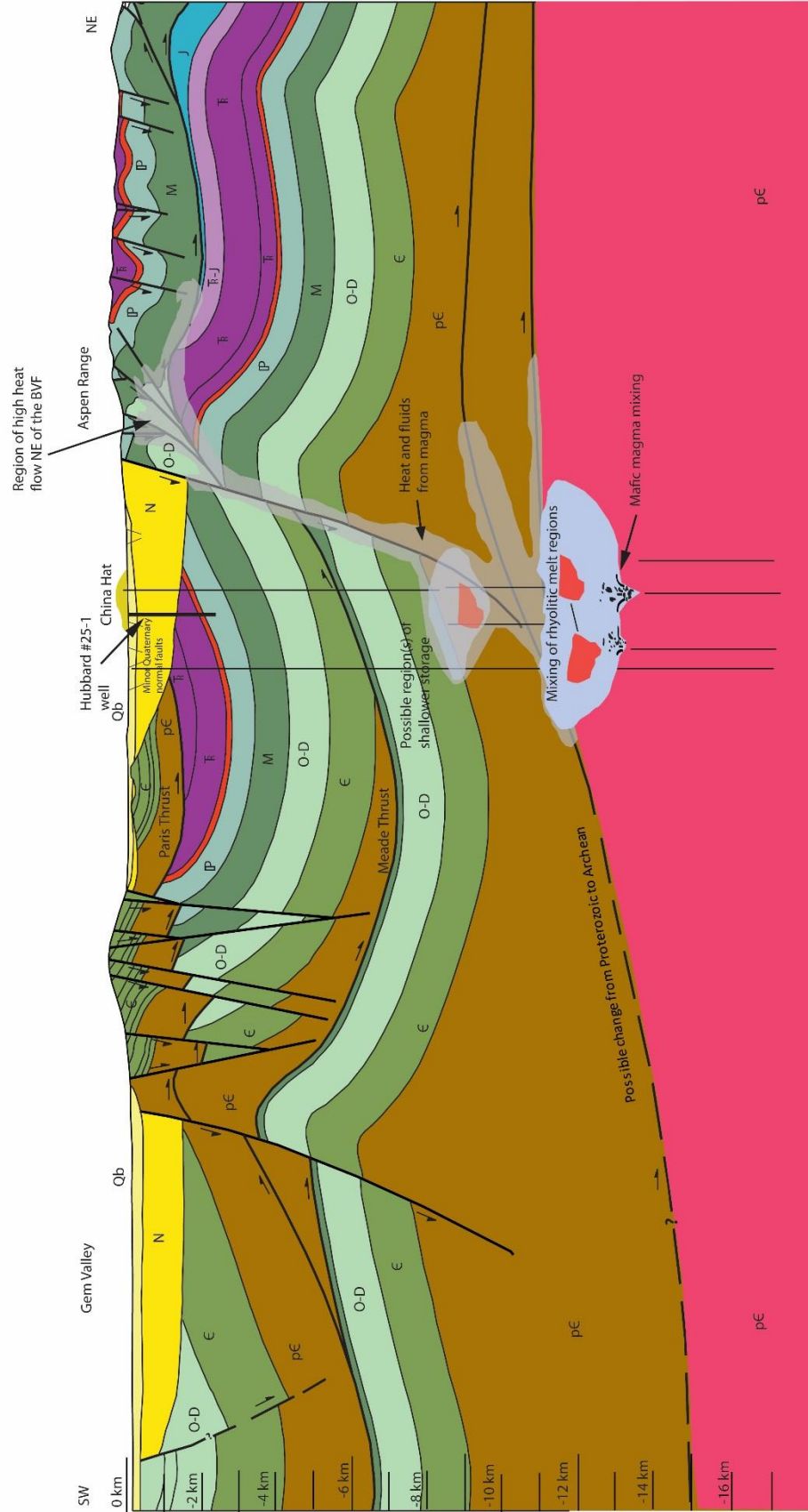


Figure 27- Conceptual model for the Blackfoot Volcanic Field. Magma storage occurs at about ~13 km depth in discrete rhyolitic regions. Heat from mafic recharge facilitates the mixing of rhyolitic regions of the magma chamber. See text for detailed discussion.

Magmatic enclaves occur in many volcanic rocks, and have been identified in other topaz rhyolites. Christiansen and Venchiarutti (1990), identified magmatic enclaves in the Spor Mountain topaz rhyolite, and mafic enclaves have been identified in the Specimen Mountain topaz rhyolite of Colorado (Christiansen et al., 1986), perhaps indicating a similar process occurring in other topaz rhyolites.

My intent with the above discussion is to emphasize the extent to which this magmatic system is dynamic. The data collected in this thesis builds upon the model that magma evolution is the culmination of many different driving processes that culminate to produce highly evolved eruptive products. This model presented here applies to the BVF directly, however magma systems are increasingly being thought of as dynamic evolving systems, often over very short time scales.

Significance for geothermal potential

Multiple studies have suggested a hot, degassing magmatic source under the BVF. The rhyolites of the BVF have been demonstrated to be a product of fractional crystallization in the mid-crust at ~13 km depth (Ford, 2005), which suggests that magma residence is not too deep contribute to upper-crustal heating in the BVF (McCurry and Welhan, 2012). Furthermore, Lewicki et al. (2012) used carbon isotopes collected from CO₂ in thermal springs near the BVF to demonstrate that a large percentage (62%) of CO₂ has a deep magmatic source, and the CO₂ emission rate is similar to that of quiescent volcanoes.

Autenrieth et al., (2011) suggested that although the BVF lacks significant surficial features indicating geothermal potential, heat and fluid transfer via faults might act to mask shallow heat signatures in the subsurface. Welhan (2016) suggests this fluid transfer along SW dipping faults may be the cause of a high heat-flow area to the NE of the BVF. Alternatively, the crustal magmatic source may be located farther to the north closer to the North Dome Field, with some lateral transfer of magma to the south under China Hat.

The revised model I present in this thesis further demonstrates the potential for geothermal development in the BVF. Mafic magma injection into the felsic reservoir as revealed from the presence of mafic magmatic enclaves shows ongoing magmatism prior to eruption of the rhyolite at 57 ka. This mafic magma has the potential of adding considerable heat to a cooler felsic reservoir at depth. Furthermore, if the different volatile concentrations of the melt inclusions represent degassing of the magma, that signifies an H₂O rich phase which transfers heat and fluids higher into the crust, which may be exploited by geothermal development.

Chapter 5: CONCLUSIONS

In an attempt to better constrain the subsurface architecture and the dynamic evolution of the China Hat topaz rhyolite I analyzed mafic enclaves and quartz-hosted melt inclusions within China Hat rhyolite system. Results from the analyses show that the mafic enclaves are the product of magma-magma interaction in a felsic magma chamber. Bulk analyses of the enclaves show variable degrees of mixing with the rhyolite, while the most primitive of the enclaves are similar to the surrounding basalts of the BVF both petrologically and geochemically. I interpret the mafic enclaves to be the product of a primitive mantle-derived basalt variably mixing with the felsic magma chamber prior to the eruption of the ~57 ka rhyolite.

Analyses of quartz-hosted melt inclusions reveal three distinct populations of melt inclusions with regards to H₂O content. The population that contains the lowest weight percent H₂O likely represents inclusions that leaked upon decompression of the rhyolite, and therefore do not well-represent pre-eruptive volatile concentrations. The two higher weight percent populations at ~2.7 and ~4.5 weight percent H₂O I interpret to recorded distinct populations of rhyolitic melt, suggesting a diverse magma plumbing-system based on geochemical differences. Normative mineral calculations suggest vapor-undersaturated crystallization, however, if the vapor bubbles in these two populations of melt inclusions represent vapor saturation, then that necessitates shallower storage in the crust than suggested by hornblende barometry. The hornblende barometry of Ford (2005) was recalculated to better use the barometer of

Johnson and Rutherford (1989). A more recent barometer (Mutch et al., 2016) was applied to Ford (2005) amphibole analyses, resulting in pressures of 3.2 ± 0.6 kbar. These pressures correspond to a depth of 12.26 ± 2.3 km, assuming a crustal density of 2.67 g/cm^3 .

The results of this thesis help to build upon a model of the magmatic underpinning of the BVF, with significance to potential geothermal development of the area. Ongoing mafic magmatism late in the development of rhyolite signifies an addition of heat into the system, which would facilitate mixing of basalts and separate rhyolitic regions of the magma chamber, the accumulation of which erupt to the surface to form the BVF. This heating may promote low degrees of partial melting of the partially solidified rhyolite, which could act to enhance the enrichment in incompatible elements driven by fractional crystallization. Furthermore, addition of mafic magma adds heat into a cooler system, which may promote the development of a productive geothermal system. Fluids and heat lost from this system may take advantage of faults, creating an area of high heat flow to the NE of the BVF.

Future work

Lithium source

Significant uncertainties are still apparent in the Blackfoot Volcanic Field system. The first one addressed here is the absence of high lithium concentrations in the melt inclusions from China Hat. Extremely enriched lithium contents in quartz-hosted melt inclusions ($>5,000$ ppm) occur in the Spor Mountain topaz rhyolite of Utah, and are

much lower in the erupted glass, suggesting large amounts of lithium can be leached from glass into surroundings (Hofstra et al., 2013). This process may be the source of Li-enriched brines associated with geothermal sites in the western United States (Hofstra et al., 2013). Furthermore, a high lithium anomaly associated with high heat flow in deep wells to the NE of China Hat suggests a source of lithium in the region (Welhan, 2016). The lithium values obtained in this thesis are not nearly as high as the Spor Mountain topaz rhyolite, however, the strong partitioning of lithium into the volatile phase could still concentrate lithium into an aqueous source, then tapped by the wells near the BVF.

Did the China Hat system ever have high lithium? Or is it a coincidence that high abundances of lithium occur in nearby wells? The sanidine Ar/Ar dates demonstrates a slightly older eruptive age for China Cap than for the North Dome and China Hat. Since only melt inclusions from the China Hat tephra were analyzed in this thesis, it is possible that with the eruption of China Cap the lithium could have been partitioned into a vapor phase associated with the eruption. Future analyses of China Cap melt inclusions could shed light on this hypothesis.

North Dome Field

Ford (2005) analyzed a limited number of samples from the Northern Dome Field (NDF), however it has been studied much less than the SDF. Does the NDF share similar sub-surface architecture with the SDF? Is the depth of storage and volatile contents similar? The region of high heat and the lithium anomaly is nearly directly under the NDF, is this significant in the context of geothermal? Further study of the NDF has

potential to unravel earlier evolutionary history of the BVF, and could place data we have on the SDF into more context.

REFERENCES

- Anders, M.H., Rodgers, D.W., Hemming, S.R., Saltzman, J., DiVenere, V.J., Hagstrum, J.T., Embree, G.F., and Walter, R.C., 2014, A fixed sublithospheric source for the late Neogene track of the Yellowstone hotspot: Implications of the Heise and Picabo volcanic fields: *Journal of Geophysical Research: Solid Earth*, v. 119, p. 2871–2906, doi: 10.1002/2013JB010483.
- Andersen, D.J., Lindsley, D.H., and Davidson, P.M., 1993, QUILF: A pascal program to assess equilibria among FeMgMnTi oxides, pyroxenes, olivine, and quartz: *Computers and Geosciences*, v. 19, p. 1333–1350, doi: 10.1016/0098-3004(93)90033-2.
- Andrews, B.J., and Manga, M., 2014, Thermal and rheological controls on the formation of mafic enclaves or banded pumice: *Contributions to Mineralogy and Petrology*, v. 167, p. 961, doi: 10.1007/s00410-013-0961-7.
- Autenrieth, K.D., McCurry, M., Welhan, J., and Polun, S., 2011, Conceptual Subsurface Model of the Blackfoot Volcanic Field, Southeast Idaho: A Potential Hidden Geothermal Resource: *Geothermal Resources Council*, v. 35, p. 695–698.
- Bachmann, O., and Bergantz, G.W., 2004, On the origin of crystal-poor rhyolites: Extracted from batholithic crystal mushes: *Journal of Petrology*, v. 45, p. 1565–1582, doi: 10.1093/petrology/egh019.
- Bachmann, O., Miller, C.F., and de Silva, S.L., 2007, The volcanic-plutonic connection as a stage for understanding crustal magmatism: *Journal of Volcanology and Geothermal Research*, v. 167, p. 1–23, doi: 10.1016/j.jvolgeores.2007.08.002.

- Le Bas, M.J., Le Maitre, R.W., Streckeisen, A., and Zanettin, B., 1986, A chemical classification of volcanic rocks based on the total alkali silica diagram: *Journal of Petrology*, v. 27, p. 745–750, doi: 10.1093/petrology/27.3.745.
- Bindeman, I.N., and Simakin, A.G., 2014, Rhyolites-Hard to produce, but easy to recycle and sequester: Integrating microgeochemical observations and numerical models: *Geosphere*, v. 10, p. 930, doi: 10.1130/GES00969.1.
- Bowen, N.L., 1928, *The evolution of the igneous rocks*: New York, NY, Dover, 334 p p.
- de Campos, C.P., Perugini, D., Ertel-Ingrisch, W., Dingwell, D.B., and Poli, G., 2011, Enhancement of magma mixing efficiency by chaotic dynamics: An experimental study: *Contributions to Mineralogy and Petrology*, v. 161, p. 863–881, doi: 10.1007/s00410-010-0569-0.
- Christiansen, E.H., and McCurry, M., 2008, Contrasting origins of Cenozoic silicic volcanic rocks from the western Cordillera of the United States: *Bulletin of Volcanology*, v. 70, p. 251–267, doi: 10.1007/s00445-007-0138-1.
- Christiansen, E.H., Sheridan, M.F., and Burt, D.M., 1986, *The Geology and Geochemistry of Cenozoic Topaz Rhyolites from the Western United States*: Geological Society of America Special Paper, v. 205, p. 82, <http://specialpapers.gsapubs.org/content/205/1.abstract> (accessed April 2015).
- Christiansen, E.H., and Venchiarutti, D. a., 1990, Magmatic inclusions in rhyolites of the Spor Mountain Formation, western Utah: Limitations on compositional inferences from inclusions in granitic rocks: *Journal of Geophysical Research*, v. 95, p. 17717, doi: 10.1029/JB095iB11p17717.

- Crittenden, M.D., 1972, Willard thrust and the Cache Allochthon, Utah: Bulletin of the Geological Society of America, v. 83, p. 2871–2880, doi: 10.1130/0016-7606(1972)83[2871:WTATCA]2.0.CO;2.
- Dayvault, R., Rush, S., and Ludlam, J., 1984, Reports on Field Investigations of Uranium Anomalies: v. 1.
- DeNosaquo, K.R., Smith, R.B., and Lowry, A.R., 2009, Density and lithospheric strength models of the Yellowstone-Snake River Plain volcanic system from gravity and heat flow data: Journal of Volcanology and Geothermal Research, v. 188, p. 108–127, doi: 10.1016/j.jvolgeores.2009.08.006.
- Didier, J., and Barbarin, B., 1991, Enclaves and granite petrology: Elsevier Science, v. 33, 626 p., doi: 10.1016/0012-8252(92)90069-6.
- Dingwell, D.B., 1990, Effects of structural relaxation on cationic tracer diffusion in silicate melts: Chemical Geology Elsevier Science Publishers B.V, v. 82, p. 209–216.
- Dixon, J.S., 1982, Regional structural synthesis, Wyoming salient of Western Overthrust belt.: American Association of Petroleum Geologists Bulletin, v. 66, p. 1560–1580, doi: 10.1306/03B5A98A-16D1-11D7-8645000102C1865D.
- Fiesinger, D.W., Perkins, W.D., and Puchy, B.J., 1982, Mineralogy and Petrology of Tertiary-Quaternary Volcanic Rocks in Caribou County, Idaho, *in* Bonnicksen, B. and Breckenridge, R.M.. eds., Cenozoic Geology of Idaho, Idaho Bureau of Mines and Geology Bulletin 26, p. 465–488.
- Ford, M.T., 2005, The petrogenesis of Quaternary rhyolite domes in the bimodal Blackfoot Volcanic Field: Idaho State University, 133 p.

- Foster, D.A., Mueller, P.A., Mogk, D.W., Wooden, J., and Vogl, J.J., 2006, Proterozoic evolution of the western margin of the Wyoming craton: implications for the tectonic and magmatic evolution of the northern Rocky Mountains: *Canadian Journal of Earth Science*, v. 43, p. 1601–1619, doi: 10.1139/e06-052.
- Ganske, R.R., 2006, the Geology and Petrology of the East Butte Area, Bingham County, Idaho:
- Ganske, R., and McCurry, M., 2007, Petrogenesis of A-type Quaternary Rhyolite and Cogenetic Mafic Magmatic Enclaves at East Butte Volcanic Dome, Eastern Snake River Plain, Idaho, *in* Proceedings of the 2005 Great Rift Science Symposium, Idaho Museum of Natural History Publication, p. 49–55.
- Hammarstrom, J.M., and Zen, E., 1986, Aluminum in hornblende: an empirical igneous geobarometer.: *American Mineralogist*, v. 71, p. 1297–1313.
- Heumann, A., 1999, Timescales of processes within silicic magma chambers.
- Hofstra, a. H., Todorov, T.I., Mercer, C.N., Adams, D.T., and Marsh, E.E., 2013, Silicate melt inclusion evidence for extreme pre-eruptive enrichment and post-eruptive depletion of lithium in silicic volcanic rocks of the Western United States: Implications for the origin of Lithium-Rich Brines: *Economic Geology*, v. 108, p. 1691–1701, doi: 10.2113/econgeo.108.7.1691.
- Holland, T., and Blundy, J., 1994, Non-ideal interactions in calcic amphiboles and their bearing on amphibole-plagioclase thermometry: *Contributions to Mineralogy and Petrology*, v. 116, p. 433–447.
- Johnson, M.C., and Rutherford, M.J., 1989, Experimental calibration of the aluminum-hornblende geobarometer with application to Long-Valley Caldera

(California) volcanic-rocks: *Geology*, v. 17, p. 837–841, doi: 10.1130/0091-7613(1989)017<0837:ecotai>2.3.co;2.

Karlstrom, K.E., Whitmeyer, S.J., Dueker, K., Williams, M.L., Bowring, S.A., Levander, A., Humphreys, E.D., and Keller, G.R., 2005, the Cd-Rom Experiment: 4-D Image of the Lithosphere Beneath the Rocky Mountains and Implications for Understanding the Evolution of Continental Lithosphere: The Rocky Mountain Region: An Evolving Lithosphere Geophysical Monograph, v. 154, <http://onlinelibrary.wiley.com/doi/10.1029/154GM31/summary>.

Kuntz, M.A., Skipp, B., Lanphere, M.A., Scott, W.E., Pierce, K.L., Dalrymple, G.B., Champion, D.E., Embree, G.F., Page, W.R., Morgan, L.A., Smith, R.P., Hackett, W.R., and Rodgers, D.W., 1994, Geologic map of the Idaho National Engineering Laboratory and adjoining areas, Eastern Idaho; http://ngmdb.usgs.gov/Prodesc/proddesc_10237.htm.

Leeman, W.P., 1982, Olivine Tholeiitic Basalts of the Snake River Plain, Idaho, *in* *Cenozoic Geology of Idaho*, p. 181–191.

Lewicki, J.L., Hilley, G.E., Dobeck, L., McLing, T.L., Kennedy, B.M., Bill, M., and Marino, B.D. V, 2012, Geologic CO₂ input into groundwater and the atmosphere, Soda Springs, ID, USA: *Chemical Geology*, v. 339, p. 61–70, doi: 10.1016/j.chemgeo.2012.06.013.

Link, P.K., Christie-Blick, N., Devlin, W.J., Elston, D.P., Horodyski, R.J., Levy, M., Miller, J.M.G., Pearson, R.C., Prave, A., Stewart, J.H., Winston, D., Wright, L.A., and Wrucke, C.T., 1993, Middle and Late Proterozoic stratified rocks of the western US Cordillera, Colorado Plateau, and Basin and Range province: *The Geology of*

- North America, v. 2, p. 463–595.
- Lochridge, W., 2016, Constraining the Petrogenesis of the Quaternary Topaz Rhyolite Lava Domes in the Bimodal Blackfoot Volcanic: Idaho State University.
- Lowenstern, J.B., 1995, Applications of silicate-melt inclusions to the study of magmatic volatiles: Magmas, Fluids and Ore Deposits. Mineralogical Association of Canada Short Course, v. 23, p. 71–99.
- Lowenstern, J.B., 1994, Dissolved volatile concentrations in an ore-forming magma: *Geology*, v. 22, p. 893–896, doi: 10.1130/0091-7613(1994)022<0893:DVCIAO>2.3.CO.
- Lowenstern, J.B., 2003, Melt Inclusions Come of Age: Volatiles, Volcanoes, and Sorby's Legacy: *Developments in Volcanology*, p. 1–21.
- Luedke, R.G., and Smith, R.L., 1983, Map showing distribution, composition, and age of late Cenozoic volcanic centers in Idaho, western Montana, west-central South Dakota, and northwestern Wyoming: U.S. Geological Survey Miscellaneous Investigations Map I-1901-E,.
- Mabey, D., and Oriel, S., 1970, Gravity and Magnetic Anomalies in the Soda Springs Region, Southeastern Idaho: U.S. Geological Survey Professional Paper 646-E, p. E1–E15.
- Mansfield, G., 1927, Geography, geology, and mineral resources of part of southeastern Idaho, with descriptions of Carboniferous and Triassic fossils: Professional Paper, p. 453 p.
- McCurry, M., Hayden, K.P., Morse, L.H., and Mertzman, S., 2008, Genesis of post-hotspot, A-type rhyolite of the Eastern Snake River Plain volcanic field by

- extreme fractional crystallization of olivine tholeiite: *Bulletin of Volcanology*, v. 70, p. 361–383, doi: 10.1007/s00445-007-0143-4.
- McCurry, M., Pearson, D., Welhan, J., Natwotniak, S.K., and Fisher, M., 2015, Origin and potential geothermal significance of China Hat and other late Pleistocene topaz rhyolite lava domes of the Blackfoot volcanic field, SE Idaho: *GRC Transactions*, v. 39, p. 35–48.
- McCurry, M., and Welhan, J., 2012, Do Magmatic-Related Geothermal Energy Resources Exist in Southeast Idaho ? *GRC Transactions*, v. 36, p. 699–707.
- Molina, J.F., Moreno, J.A., Castro, A., Rodr??guez, C., and Fershtater, G.B., 2015, Calcic amphibole thermobarometry in metamorphic and igneous rocks: New calibrations based on plagioclase/amphibole Al-Si partitioning and amphibole/liquid Mg partitioning: *Lithos*, v. 232, p. 286–305, doi: 10.1016/j.lithos.2015.06.027.
- Morgan, W.J., 1971, Convection Plumes in the Lower Mantle: *Nature*, v. 230, p. 42–43, doi: 10.1038/230042a0.
- Mueller, P. a., Wooden, J.L., Mogk, D.W., and Foster, D. a., 2011, Paleoproterozoic evolution of the Farmington zone: Implications for terrane accretion in southwestern Laurentia: *Lithosphere*, v. 3, p. 401–408, doi: 10.1130/L161.1.
- Mutch, E.J.F., Blundy, J.D., Tattitch, B.C., Cooper, F.J., and Brooker, R.A., 2016, An experimental study of amphibole stability in low-pressure granitic magmas and a revised Al-in-hornblende geobarometer: *Contributions to Mineralogy and Petrology*, v. 171, p. 1–27, doi: 10.1007/s00410-016-1298-9.
- Nekvasil, H., and Burnham, C.W., 1987, The calculated individual effects of pressure

- and water content on phase equilibria in the granite system: The Geochemical Society, Special Publications, v. 1, p. 433–445.
- Payne, S.J., McCaffrey, R., King, R.W., and Kattenhorn, S.A., 2012, A new interpretation of deformation rates in the Snake River Plain and adjacent basin and range regions based on GPS measurements: *Geophysical Journal International*, v. 189, p. 101–122, doi: 10.1111/j.1365-246X.2012.05370.x.
- Peng, X., and Humphreys, E.D., 1998, Crustal velocity structure across the eastern Snake River Plain and the Yellowstone swell: *Journal of Geophysical Research*, v. 103, p. 7171–7186, doi: 10.1029/97JB03615.
- Pickett, K.E., 2004, *Physical Volcanology , Petrography , and Geochemistry of Basalts in the Bimodal Blackfoot Volcanic Field , Southeastern Idaho*: Idaho State University, 92 p.
- Pierce, K.L., and Morgan, L.A., 2009, Is the track of the Yellowstone hotspot driven by a deep mantle plume? - Review of volcanism, faulting, and uplift in light of new data: *Journal of Volcanology and Geothermal Research*, v. 188, p. 1–25, doi: 10.1016/j.jvolgeores.2009.07.009.
- Pierce, K.L., and Morgan, L.A., 1992, The track of the Yellowstone hot spot: Volcanism, faulting, and uplift: *Geological Society of America Memoirs*, v. 179, p. 1–54, doi: 10.1130/MEM179-p1.
- Polun, S.G., 2011, *Kinematic Analysis of Late Pleistocene Faulting in the Blackfoot Lava Field, Caribou County, Idaho*: Idaho State University, 86 p.
- Preece, K., Gertisser, R., Barclay, J., Berlo, K., and Herd, R. a., 2014, Pre- and syn-eruptive degassing and crystallisation processes of the 2010 and 2006

- eruptions of Merapi volcano, Indonesia: Contributions to Mineralogy and Petrology, v. 168, p. 1061, doi: 10.1007/s00410-014-1061-z.
- Ridolfi, F., and Renzulli, A., 2012, Calcic amphiboles in calc-alkaline and alkaline magmas: Thermobarometric and chemometric empirical equations valid up to 1,130°C and 2.2 GPa: Contributions to Mineralogy and Petrology, v. 163, p. 877–895, doi: 10.1007/s00410-011-0704-6.
- Rodgers, D.W., Ore, H.T., Bobo, R.T., Mcquarrie, N., and Zentner, N., 2002, Extension and Subsidence of the Eastern Snake River Plain, Idaho: Idaho Geological Survey Bulletin, v. 30, p. 121–155.
- Royse, F.J., Warner, M.A., and Reese, D.L., 1975, Thrust belt structural geometry and related stratigraphic problems Wyoming-Idaho-northern Utah: Rocky Mountain Association of Geologists, p. 41–54.
- Silver, L., and Stolper, E., 1985, A thermodynamic model for hydrous silicate melts: The Journal of Geology, v. 93, p. 161–178.
- Student, J.J., and Bodnar, R.J., 1996, Melt inclusion microthermometry: petrologic constraints from the H₂O-saturated haplogranite system: Petrology, v. 4, p. 291–306, <http://www.maik.ru/cgi-perl/search.pl?type=abstract&name=petreng&number=3&year=96&page=291>.
- Tuttle, O., and Bowen, N., 1958, Origin of granite in the light of experimental studies in the system NaAlSi₃O₈-KAlSi₃O₈-SiO₂-H₂O: Geological Society of America Memoirs, v. 74, p. 1–146, doi: 10.1130/MEM74-p1.
- Vernon, R.H., 2004, A Practical Guide To Rock Microstructure: Cambridge, Cambridge University Press, v. 606, doi: 10.1017/CBO9780511807206.

- Welhan, J.A., 2016, Gigawatt-Scale Power Potential of a Magma-Supported Geothermal System in the Fold and Thrust Belt of Southeast Idaho: PROCEEDINGS, 41st Workshop on Geothermal Reservoir Engineering Stanford University, v. SGP-TR-209, p. 1–13.
- Yavuz, F., 1996, AMPHCAL: A quickbasic program for determining the amphibole name from electron microprobe analysis using the IMA rules: *Computer and Geosciences*, v. 22, p. 101–107.
- Yonkee, A., 2005, Strain patterns within part of the Willard thrust sheet, Idaho-Utah-Wyoming thrust belt: *Journal of Structural Geology*, v. 27, p. 1315–1343, doi: 10.1016/j.jsg.2004.06.014.
- Yonkee, W.A., Dehler, C.D., Link, P.K., Balgord, E.A., Keeley, J.A., Hayes, D.S., Wells, M.L., Fanning, C.M., and Johnston, S.M., 2014, Tectono-stratigraphic framework of Neoproterozoic to Cambrian strata, west-central U.S.: Protracted rifting, glaciation, and evolution of the North American Cordilleran margin: *Earth-Science Reviews*, v. 136, p. 59–95, doi: 10.1016/j.earscirev.2014.05.004.
- Yonkee, W.A., and Weil, A.B., 2015, Tectonic evolution of the Sevier and Laramide belts within the North American Cordillera orogenic system: *Earth-Science Reviews*, v. 150, p. 531–593, doi: 10.1016/j.earscirev.2015.08.001.
- Yuan, H., Dueker, K., and Stachnik, J., 2010, Crustal structure and thickness along the Yellowstone hot spot track: Evidence for lower crustal outflow from beneath the eastern Snake River Plain: *Geochemistry, Geophysics, Geosystems*, v. 11, doi: 10.1029/2009GC002787.

APPENDIX

Link to Excel file with SIMS data:

SIMSworkbook.xlsx